The South Tibetan detachment system facilitates ultra rapid cooling of granulite-facies rocks in Sikkim Himalaya

Dawn A. Kellett,[1] Djordje Grujic,[2] Isabelle Coutand,[2] John Cottle,[1] and Malay Mukul[3]

Received 13 July 2012; revised 19 November 2012; accepted 14 December 2012; published 30 April 2013.

[1] The eastern Himalaya is characterized by a region of granulites and local granulitized eclogites that have been exhumed via isothermal decompression from lower crustal depths during the India-Asia collision. Spatially, most of these regions are proximal to the South Tibetan detachment system, an orogen-parallel normal-sense detachment system that operated during the Miocene, suggesting that it played a role in their exhumation. Here we use geo- and thermochronological methods to study the deformation and cooling history of footwall rocks of the South Tibetan detachment system in northern Sikkim, India. These data demonstrate that the South Tibetan detachment system was active in Sikkim between 23.6 and ~13 Ma, and that footwall rocks cooled rapidly from ~700 to ~120 °C between ~15-13 Ma. While active, the South Tibetan detachment system exhumed rocks from mid-crustal depths, but an additional heat source such as strain heating, advected melt and/or crustal thinning is required to explain the observed isothermal decompression. Cessation of movement on the South Tibetan detachment system produced rapid cooling of the footwall as isotherms relaxed. A regional comparison of temperature-time data for the eastern South Tibetan detachment system indicates a lack of synchronicity between the Sa'er-Sikkim-Yadong section and the NW Bhutan section. To accommodate this requires either strike-slip tear faulting or local out-of-sequence thrusting in the younger segment of the orogen.

Citation: Kellett, D. A., I. Coutand, J. Cottle, and M. Mukul (2013), The South Tibetan detachment system facilitates ultra rapid cooling of granulite-facies rocks in Sikkim Himalaya, *Tectonics*, *32*, 252–270, doi:10.1002/tect.20014.

1. Introduction

[2] Recent studies have identified and characterized high-grade metamorphic rocks, both granulites and granulitized eclogites, in the eastern Himalaya, delimiting a large region of high temperature (HT) and high pressure to high temperature (HP → HT) metamorphic rocks which includes southeastern Tibet, eastern Nepal, Sikkim and northwestern Bhutan [e.g. *Ganguly et al*., 2000; *Borghi et al*., 2003; *Groppo et al*., 2007; *Rolfo et al*., 2008; *Cottle et al*., 2009a; *Chakungal et al*., 2010; *Corrie et al*., 2010; *Warren et al*., 2011a; *Grujic et al*., 2011; *Gong et al*., 2011; Figure 1]. With the exception of Arun valley in Nepal, the HT and HP → HT rocks occur in close proximity to the South Tibetan detachment system (STDS), the major orogen-parallel normal-sense detachment system of the Himalayan orogen [Figure 1; *Burchfiel et al*., 1992].

[3] Miocene age estimates for peak granulite-facies metamorphism of some of the granulitized eclogites [e.g. *Cottle et al*., 2009a; *Warren et al*., 2011a] suggest exhumation from at least 30 km depth to the surface within 13 myr. PT paths of both the granulites and the granulitized eclogites are characterized by large magnitude (≥ 0.5 GPa) near-isothermal decompression during exhumation [*Groppo et al*., 2007; *Ganguly et al*., 2000; *Grujic et al*., 2011].

[4] Possible exhumation processes for HP rocks include buoyancy resulting from local density contrasts (e.g. low-density material attached to a subducting slab), and other tectonic processes including indenter or plunger-driven expulsion, driven cavity flow, and crustal scale extensional detachments [e.g. *England and Molnar*, 1990; *Ernst*, 2001; *Warren et al*., 2008]. Erosion and tectonic processes local or regional, including extension, also play a significant role during late exhumation from mid crustal levels to the surface. As density contrasts in the predominantly supracrustal lithologies present in Himalayan crust are minor, as HT and HP → HT metamorphism is recorded in mafic lenses which are denser than their host gneisses, and as the estimated pressures of HP metamorphism (≥ 1.5 GPa) do not exceed those expected at the base of the Himalayan crust, it is unlikely that the HT or HP → HT rocks in the eastern Himalaya could have been exhumed by buoyancy forces [e.g. *Warren et al*., 2011a; *Grujic et al*., 2011]. However, it is likely that tectonics played an important role in exhumation. In particular, HP → HT rocks at Ama Drime (Figure 1) are bound by both N-dipping (the STDS), and E- and W-dipping major normal fault systems that formed under different tectonic regimes. While the more shallow N-dipping STDS formed as a roof system during NS shortening and

Additional supporting information may be found in the online version of this article.

[1]Department of Earth Science, University of California, Santa Barbara, California, USA.
[2]Department of Earth Sciences, Dalhousie University, Halifax, Nova Scotia, Canada.
[3]Department of Earth Sciences, Indian Institute of Technology, Bombay, India.

Corresponding author: Dawn A. Kellett, now at Geological Survey of Canada, Ottawa, Ontario, K1A 0E8. (Dawn.Kellett@nrcan.gc.ca)

0278-7407/13/10.1002/tect.20014

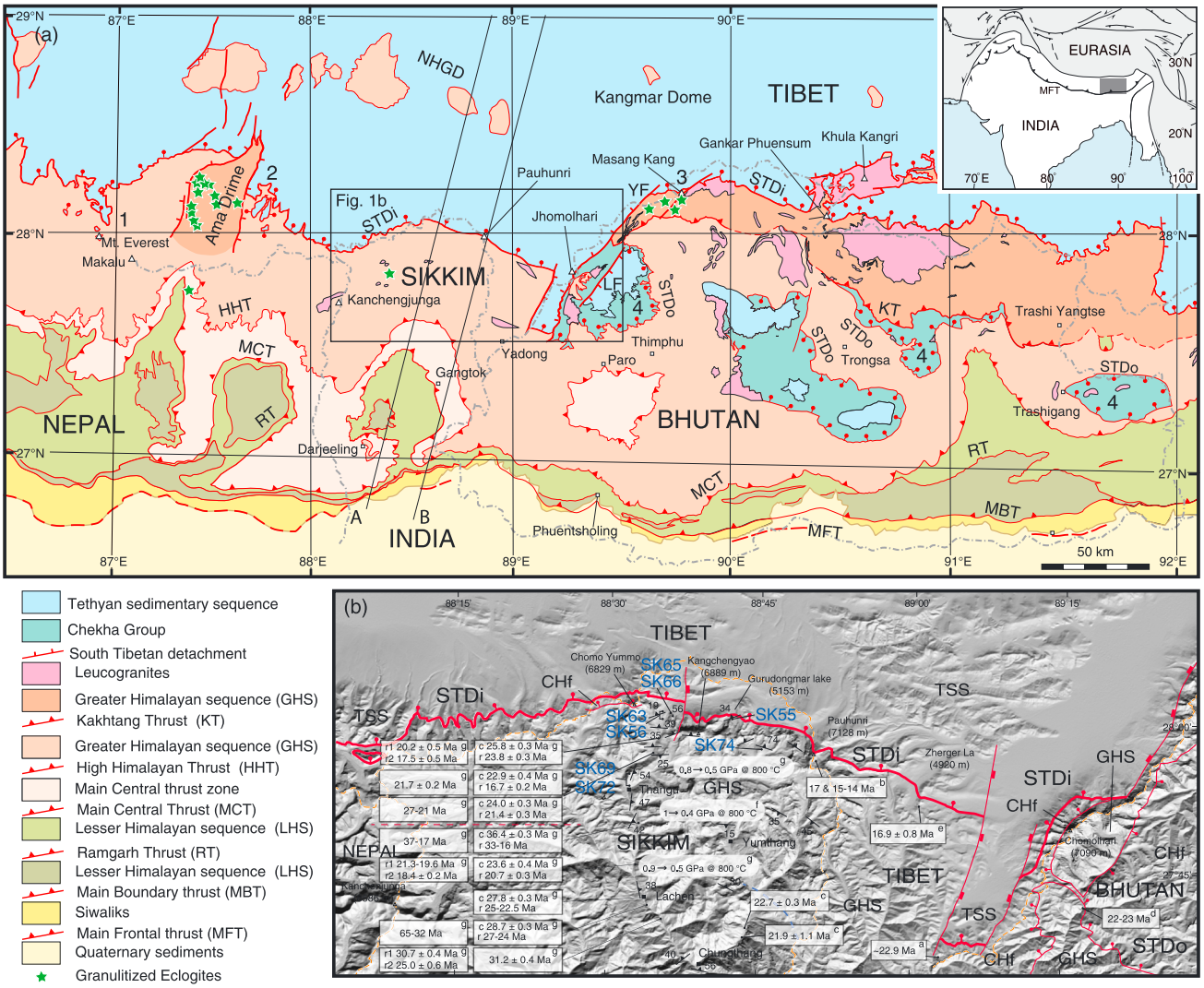

Figure 1. (a) Geological map of the eastern Himalaya (modified from *Schelling*, 1992; *Goscombe and Hand*, 2000; *Goscombe et al*., 2006; *Bhattacharyya and Mitra*, 2009; *Kali et al*., 2010; *Kellett et al*., 2010; *Grujic et al*., 2011]. NHGD: North Himalayan gneiss dome. Numbers 1 to 4 denote areas from which data in Figure 11 were obtained; see caption to Figure 11 for details. (b) Trace of the upper detachment surface of the STDS in northern Sikkim as determined by our field observations and analyses of satellite imagery. Shaded relief digital elevation model (DEM) was produced by GISmatter.com and is based on the NASA Shuttle Radar Topographic Mission (SRTM) data (resolution of 90 m at the equator, *Jarvis et al*., 2008).Trace of the STDS and other indicated shear zones and faults and foliation measurement are from *Kellett et al*. [2010] and this work. TSS – Tethyan sedimentary sequence, CHf – Chekha formation, GHS – Greater Himalayan sequence, STDi – inner STD system, STDo – outer STD system [as described in *Kellett and Grujic*, 2012]. SK55-SK74 samples are described in this paper. Published geochronological data are from: (a) *Wu et al*., 1998; (b) *Edwards et al*., 2002; (c) *Catlos et al*., 2004; (d) *Kellett et al*., 2009; (e) *Gong et al*., 2011, and; (g) *Rubatto et al*., 2012; r and c denote rim and core spots, r1 and r2 are different rim locations. Red dashed line separates samples from two structural levels. Monazite data are in italics, zircon data in plain text. Published thermobarometric data (f) are from *Ganguly et al*., 2000 and (g) *Rubatto et al*., 2012. Foliation measurements are our observations as well as from *Neogi et al*. [1998]. Cross sections corresponding to lines AA' and BB' are in Figure 2.

southward extrusion of the midcrust, the steeper E- and W-dipping structures formed subsequently, as a result of EW extension of the orogen. It has been proposed that the later EW extensional structures are the major exhumation structures for the HP→HT rocks [e.g. *Cottle et al*., 2009a; *Jessup et al*., 2008; *Kali et al*., 2010]. In contrast, HP → HT rocks in NW Bhutan are proposed to have been exhumed by extrusion between coeval normal (STDS) and thrust-sense shear zones, following ramping over previously extruded rocks [e.g. *Warren et al*., 2011a; *Grujic et al*., 2011]. While the first hypothesis implies a short, near-vertical exhumation path during crustal thinning and stretching, the second implies a

longer exhumation path with significant lateral displacement during crustal shortening and thickening.

[5] In order to examine these hypotheses regarding the exhumation mechanisms in this region of the Himalaya, we focus on the STDS, which plays a key role in proposed exhumation models for both Ama Drime and NW Bhutan HP HT rocks. In Sikkim, India, situated between Ama Drime and NW Bhutan, granulite-facies rocks occurring just south of the STDS have been well-studied [e.g. *Neogi et al*., 1998; *Ganguly et al*., 2000; *Dasgupta et al*., 2004], and HP → HT rocks have been recently identified [*Rolfo et al*., 2008]. The lack of documented E- and W-dipping normal faults leads us to infer that exhumation in Sikkim was facilitated solely by the orogen-parallel STDS. To determine the timing of displacement on the STDS and the thermal history of its footwall, we use the U-Th-Pb, Ar-Ar, fission track and (U-Th)/He dating techniques and accessory phase chemistry.

2. Geological Setting

2.1. Himalayan Orogen

[6] The Himalaya-Tibet orogen is the result of the continental collision of India with Asia, involving closure of the intervening Tethyan Ocean at ~55-50 Ma [*Rowley*, 1996; *DeCelles et al*. 2004; *Green et al*. 2008]. The southern flank of the orogen, which is hereafter referred to as the Himalaya, or the Himalayan orogen, is a large-scale system of predominantly north-dipping structures. These structures affect upper and mid-crustal rocks (Figure 1), whose protoliths were originally deposited as part of a southward-tapering supracrustal sedimentary wedge on the northern margin of the Indian continent [e.g. *Long et al*., 2011a].

[7] The broad central arc of the Himalaya is characterized by a series of fault-separated lithotectonic units (Figure 1; *Le Fort*, [1975]). The northernmost lithotectonic assemblage, the Tethyan sedimentary sequence (TSS) is bounded to the north by the Indus-Tsangpo suture [e.g. *Hébert et al*., 2012], the boundary between the Indian and Asian continents, and to the south by a network of top-down-to-the-north shear zones and brittle faults, the STDS [*Burchfiel et al*., 1992]. Geophysical and geologic data indicate that the deepest components of the STDS sole out into the upper- to mid-crust [e.g. *Nelson et al*. 1996; *Hauck et al*., 1998; *Lee et al*., 2000; *Wagner et al*., 2010] potentially connecting further north to the basal detachment of a pre-Miocene south-vergent fold and thrust belt [e.g. *Ratschbacher et al*., 1994]. The footwall of the STDS consists of high-grade metamorphic rocks of the Greater Himalayan series (GHS). Structurally below the GHS, and separated from it by the Main Central thrust (MCT), lies the lower- to upper-greenschist facies Lesser Himalayan series (LHS). The lower boundary of the LHS is the Main Boundary thrust (MBT), which separates it from the Subhimalaya, the deformed foreland basin of the orogen. The youngest and most external thrust of the Himalayan orogen is the active Main Frontal thrust (MFT) [e.g. *Lavé and Avouac*, 2000].

[8] Cenozoic metamorphism recorded in the GHS, is characterized by rarely-preserved prograde kyanite-stable metamorphism caused by crustal thickening during Eocene to Late Oligocene [*Hodges et al*. 1996, *Godin et al*. 2001; *Catlos et al*., 2002; *Cottle et al*. 2009b; *Larson et al*. 2010], and by sillimanite-stable metamorphism, partial melting and exhumation of rocks from depths corresponding to 10–12 kbar to the southern Himalayan topographic front in Early to Middle Miocene [*Vannay and Hodges* 1996, *Hodges et al*. 1996; *Godin et al*. 2006 and references therein; *Cottle et al*. 2009a, 2009b; *Kellett et al*. 2010] and even younger prograde metamorphism at lower structural levels [e.g. *Harrison et al*., 1997]. In addition, there is mounting evidence that the base of the crust beneath southern Tibet is eclogitized [*Hetényi et al*., 2007] and that for some portions of the GHS in the eastern Himalaya eclogite-facies metamorphism was concurrent with amphibolite-facies metamorphism in the mid-crust during the Early and Middle Miocene [*Corrie et al*., 2010; *Grujic et al*., 2011; *Warren et al*., 2011a, 2011b]. HP metamorphism was succeeded by Middle Miocene granulite-facies HT metamorphism [e.g. *Cottle et al*., 2009a; *Warren et al*., 2011a, 2011b].

[9] The STDS was first described by *Burg and Chen* [1984] and *Burg et al*. [1984] as a normal fault that deformed leucogranites at the top of the GHS metamorphic package, and that in places juxtaposed low-grade metamorphosed Jurassic schists against staurolite-kyanite gneiss. Investigating crystallographic preferred orientations in quartz crystals within leucogranites in southern Tibet east of Bhutan, *Burg et al*. [1984] demonstrated that the upper boundary of the GHS was a shear zone of gently-dipping mylonite gneisses hundreds of metres thick that had an opposite shear sense to the regional thrusting. They further demonstrated that shearing post-dated emplacement of the leucogranites, which at that time were already suspected to be produced from partial melting within the GHS above the MCT. This timing relationship demonstrated that the normal-sense structure was likely Miocene in age, and thus potentially coeval to either the MCT or the MBT. Burg and colleagues noted the apparent incongruity of a north-directed normal-sense ductile shear zone within the south-directed thrust-sense Himalayan orogen, and explained its formation by sliding of the TSS along a gravity-driven detachment [*Burg et al*., 1984]. Most subsequent hypotheses about the formation of the STDS consider it to be synchronous with the MCT.

[10] Since *Burchfiel et al*. [1992]'s follow-up comprehensive study of the detachment system it has been recognized that the STDS typically comprises two structures, a diffuse, low-angle ductile shear zone cut by a discrete and structurally-higher ductile/brittle shear zone [see review in *Kellett and Grujic*, 2012]. Hypotheses about the formation of the detachment system include ductile channel flow followed by extrusion [e.g. *Jamieson et al*., 2004; *Kellett and Grujic*, 2012]; tectonic wedging [e.g. *Webb et al*., 2007; 2011] and; gravity-driven flattening and/or slip [e.g. *Burchfiel and Royden*, 1985; Corrie *et al*., 2012].

2.2. Geology of Sikkim, India

[11] The structure of the Sikkim Himalaya consists, from structurally-highest to structurally-lowest, of: the STDS, MCT II and MCT I structures which bracket the MCT zone (in some publications the numbers of those structures are reversed), the Ramgarh thrust (exposed both in the Rangit window and towards the foreland), MBT and related reactivation thrusts, and MFT [*Gansser*, 1964; *Mukul*, 2000; *Dasgupta et al*., 2004; *Bhattacharyya and Mitra*, 2009, 2011; Figures 1 and 2]. The map pattern is dominated by the arcuate surface traces

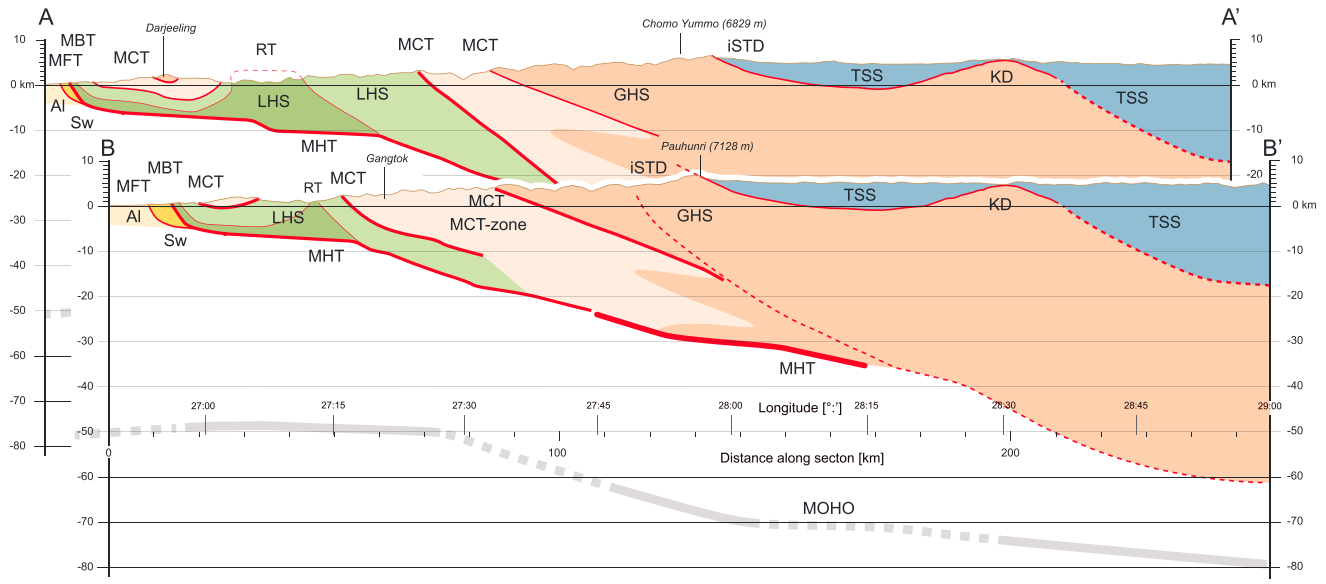

Figure 2. Cross sections AA' and BB' (legend and locations indicated in Figure 1). The structures at depth are constrained by geophysical data [*Acton et al*., 2011; *Mitra et al*., 2005; *Alsdorf et al*., 1998; *Hauck et al*., 1998] and cross sections by *Bhattacharyya and Mitra* [2009], *Quigley et al*. [2008]; *Ratschbacher et al*. [1994]. Al—Aluvial sediments; GB—Gangdese batholith; GHS—Greater Himalayan sequence; iSTD—inner South Tibetan Detachment system; LHS—Lesser Himalayan sequence; MBT—Main Boundary thrust; MCT—Main Central thrust; MFT—Main Frontal thrust; MHT—Main Himalayan thrust; RT—Ramgarh thrust; SW—Siwalik sediments; TSS—Tethyan sedimentary sequence.

of the MCT structures and exposure of the MCT zone, cored by a duplex of LHS metasedimentary rocks in the Sikkim or Tista window [e.g. *Dasgupta et al*., 2004].

[12] Metapelites in the upper portion of the GHS reached granulite-facies peak metamorphic conditions of 0.8-0.9 GPa and ~800 °C, and monazite and zircon associated with partial melting indicate that melt was widespread and diachronous between 31–17 Ma [*Rubatto et al*., 2012]. In particular, *Rubatto et al*. [2012] found that higher structural levels preserve evidence of later melting (~26-23 Ma) than lower structural levels (~31-27 Ma), marking a tectonic discontinuity at about the level of the village of Thanggu (Figure 1b). Monazite from within the MCT zone (between MCT I and MCT II) in Sikkim has yielded Th-Pb ages between 22–10 Ma [*Catlos et al*., 2004], and is interpreted to have grown during progressive/intermittent motion on the MCT system throughout the Early and Middle Miocene. Sm-Nd geochronology of garnets collected from the hanging wall of the MCT zone yielded 23 ± 3 Ma and 16 ± 2 Ma, and is interpreted as dating prograde garnet growth and near-peak T melting, respectively [*Harris et al*., 2004]. Monazite from the deformed Pauhunri leucogranite stockwork located beneath the STDS [*Edwards et al*., 2002] yielded Th-Pb ages of 17 and 15–14 Ma, which may reflect melting episodes, or possibly fluid flow during slip on the detachment [*Catlos et al*., 2004]. Further east in the Yadong area, mafic granulites in the footwall of the STDS yielded zircon U-Pb ages of 16.9 ± 0.8 Ma [*Gong et al*., 2011]. *Wu et al*. [1998] report a monazite ^{235}U-^{207}Pb TIMS age of ~22.9 Ma (but recognize an undefined inherited component) from the little-deformed Gaowu granite hosted by TSS phyllite and schist. Conversely, the phyllite and schist host rocks may correlate along strike with Chekha Group rocks of Bhutan [*Gansser*, 1983], which would situate the Gaowu granite within but not above the STDS, similar to and along strike of the Chung La granite as shown in Figure 1b [e.g. *Kellett et al*., 2009; 2010].

2.3. South Tibetan Detachment System in Sikkim

[13] The STDS in Sikkim and Zherger La (Figure 1b) is a well-exposed composite of two structures exposed north of the village of Thanggu: a diffuse ductile low-angle zone of top-to-the-north shear that deformed paragneiss and orthogneiss, cut by a ductile-brittle to brittle normal-sense fault that dips more steeply to the north [*Wu et al*., 1998; *Edwards et al*., 2002; our observations; Figure 3g]. Hanging wall rocks of the upper structure include Devonian-Jurassic carbonates and clastics [*Wu et al*., 1998; *Edwards et al*., 2002]. In northwestern Sikkim, a thin sliver of Neoproterozoic-Cambrian slate and schist intercalated with sandstone, quartzite and/or marble has also been mapped [*Pan et al*., 2004], which may correlate with the marbles, phyllite and schist mapped north of the Gaowu granite of *Wu et al*. [1998]. Its described age and lithology bear similarity to rocks in similar structural position to the east, the Chekha Group in Bhutan [*Gansser*, 1983] and west, the Everest Series in eastern Nepal [e.g. *Searle et al*., 2003]. The footwall rocks include partially-migmatitic garnet-biotite-sillimanite paragneiss and feldspar augen gneiss, with local mafic lenses, pervasively cut by variably-deformed leucogranite and aplite dykes and sills (Figure 3g).

3. Geochronology and Geochemistry

[14] A suite of samples was collected from both leucogranite bodies and their host metamorphic rocks in order to constrain the timing of metamorphism and ductile deformation in the footwall of the STDS (Table 1). Samples were collected from

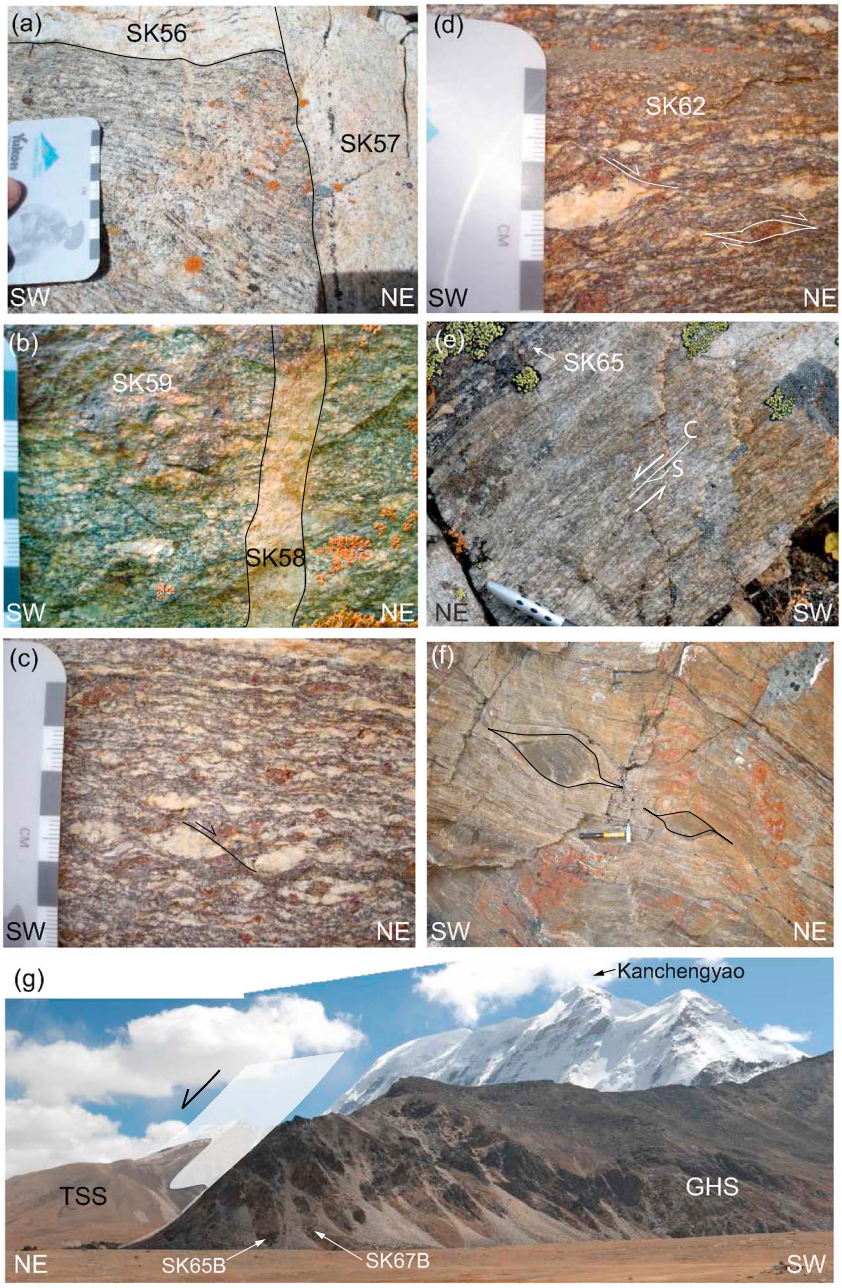

Figure 3. Outcrop photos of studied samples. (a) SK56 leucosome in migmatite gneiss, crosscut by SK57 leucogranite dyke. (b) Host rock is SK59 mylonite gneiss, cross-cut by 1–2 cm-thick SK58 aplite dyke. (c) Top-down-to-NE shear bands cutting leucosomes in garnet-bearing migmatite gneiss. (d) Top-down-to-NE shear bands and asymmetric pressure shadows around garnet in migmatite gneiss, SK62. (e) S-C' fabric in SK65 mylonite gneiss. (f) Mafic dykes have been boudinaged, here forming s-type clasts with top-down-to-northeast shear sense. (g) Panoramic view of the STDS in Sikkim. Fissile weathered black shale of the TSS is visible in the hanging wall of the ductile-brittle shear zone to the NE. Rocks in the footwall are resistant, blocky high-grade migmatitic gneiss and mylonite gneiss of the GHS, pervasively deformed within the STDS diffuse ductile shear zone with top-NE shear fabric. The distance between samples sites for SK65B and SK67B is ~75 m.

within the top-to-the-north deformation zone of the STDS north of the village of Thanggu.

3.1. Zircon

3.1.1. Sample Descriptions, Preparation, and Methodology

[15] Five leucogranite samples were selected for zircon U-Pb geochronology, trace element geochemistry and Ti-in-zircon thermometry using the SHRIMP-RG (sensitive high-resolution ion microprobe-reverse geometry) operated at Stanford University. Mineral separation, zircon cathodoluminescence (CL) images, trace element patterns and analytical procedures are outlined in Appendix A of the supplementary material. Sample locations are shown in Figure 1b. These samples

Table 1. Sample coordinates, description and analyses performed[a]

Sample	Latitude	Longitude	Rock type	U-Pb zircon	Ti-in-zircon	U-Th-Pb monazite	$^{40}Ar/^{39}Ar$ muscovite	FT apatite	(U-Th)/He apatite
SK 55	28°00.572′ N	88°42.402′ E	leucogranite					X	X
SK 56	28°00.886′ N	88°35.566′ E	leucosome	X	724-840 °C		X		
SK 57	28°00.886′ N	88°35.566′ E	leucogranite	X	643-797 °C		X		
SK 58	28°00.963′ N	88°35.569′ E	aplite	X	692-790 °C		X		
SK 60	28°01.036′ N	88°35.585′ E	granite	X	576-818 °C				
SK 62	28°01.070′ N	88°35.588′ E	gneiss			X			
SK 65B	28°01.176′ N	88°36.274′ E	mylonite gneiss			X			
SK 67B	28°01.139′ N	88°36.252′ E	mylonite gneiss			X			
SK 69	27°54.713′ N	88°32.199′ E	gneiss					X	
SK 70	27°54.400′ N	88°32.169′ E	migmatite gneiss					X	
SK 71	27°54.283′ N	88°32.211′ E	migmatite gneiss					X	
SK 72	27°54.062′ N	88°32.208′ E	leucogranite					X	
SK 74	27°57.655′ N	88°45.501′ E	leucosome	X	663-771 °C		X		

[a]Detailed analyses for the samples are provided in the online Supporting Information.

were selected because they preserved a range of cross-cutting relationships with the host mylonite gneiss.

[16] SK 56 is a deformed Qtz + Pl + Sil + Bt + Ms leucosome with a weak S fabric hosted by migmatite gneiss (Figures 3a and 4a, mineral abbreviations are according to *Whitney and Evans*, [2010]). SK 57 is a deformed Qtz + Pl + Ks + Bt + Ms leucogranite that cross-cuts SK 56 and its host gneiss (Figure 3a). It lacks both S and L fabrics (Figure 4b). SK 58 is a fine-grained Qtz + Pl + Ms + Tu + Grt aplite dyke that cross-cuts mylonite gneiss at a high angle (Figure 3b). Quartz grains in the aplite dyke are weakly deformed by bulging and subgrain rotation crystallization, but there is no pervasive fabric. The sharp boundaries of the dyke indicate that its emplacement post-dates mylonite development in the host

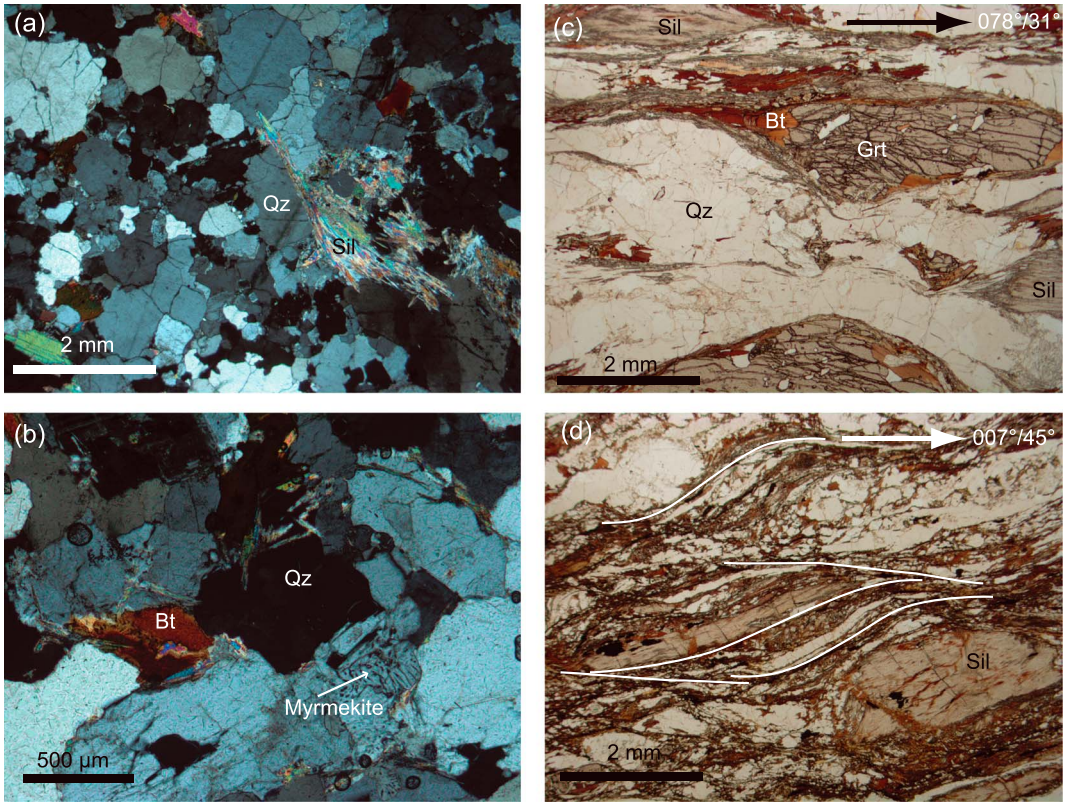

Figure 4. Plane-polarized (PP) and cross-polarized (XP) light photographs of thin sections for selected samples from this study. (a) SK56, sillimanite-bearing leucosome in migmatite gneiss, with grain size reduction in quartz, shown under crossed polarizers (XP). (b) SK57, weakly-deformed leucogranite that cross-cuts SK56 (XP). Myrmekite texture in feldspar is visible. Weak preferred orientation of crystals is evident at lower magnification. (c) SK62, Grt-Bt-Sil-bearing gneiss. (d) SK65A mylonite gneiss with coarse mats of sillimanite and fine-grained quartz and mica matrix. S-C fabric is outlined. Mineral abbreviations after Whitney and Evans, 2010.

gneiss. SK 60 is a coarse-grained cordierite-bearing leucogranite with Pl + Qtz + Ks + Bt + Ms. It is deformed with an S fabric defined by the plane-parallel alignment of biotite, muscovite and quartz. SK 74 is a large, non-foliated leucosome containing both Ms and Tu.

[17] Zircons in SK 56 range from elongate- to stubby-columnar. Most grains have bright-under-CL cores, and are often oscillatorily-zoned, with thin dark-under-CL rims, while a few grains have mottled, dark-under-CL cores with thin oscillatory-zoned dark-under-CL rims. SK 57 zircons have aspect ratios of ~3:2. They have complexly-zoned cores enveloped by oscillatory-zoned rims. The rims are thin (~25 μm wide) and dark under CL. SK 58 zircons are sub-rounded. Rounded and abraded cores are enveloped by thick (≥50 μm) dark-under-CL rims with oscillatory zoning. SK 60 grains vary from large and elongate to small and sub-rounded. There is no consistent morphology, but most grains have distinct rims and cores. SK 74 grains range from ~500 to <100 μm in length. Most cores display oscillatory zoning, and most rims are thin and dark-under-CL.

[18] Approximately 20–40 spots from 15–25 zircon grains were analyzed for each sample, including representative core and rim analyses, and emphasizing rim analyses where possible. Analysis pits were ~25 μm in diameter with a depth of ~1-2 μm.

3.1.2. Zircon U-Pb Geochronology Results

[19] Zircons from all samples analyzed possessed inherited cores and Tertiary overgrowths (Figure 5; Supporting Information, Table S1). SK 56 yielded a population of ca. 500 Ma and few ca. 800 Ma cores. SK 57 cores yield a discordia line between ca. 1900 and 850–800 Ma populations. SK 58 cores include a small slightly discordant population of ca. 2500 Ma cores which could be tied along a discordia line to either ca. 900 Ma concordant or ca. 500 Ma discordant cores. SK 60 zircons contain a ca. 800 Ma population with few discordant ca. 1850 Ma cores. SK 74 zircon cores are predominantly ca. 800 Ma, with few discordant ca. 550 Ma cores, and one discordant core each of ca. 1800 Ma and ca. 2500 Ma. Note that core data are not plotted, but are included in Supporting Information, Table S1.

[20] For all samples analyzed, zircon rims are Tertiary and yield a spread of ages ≥ 8 myr along concordia (Figure 5). The spread of ages may be a result of protracted crystallization of zircon rims during protracted melting [*Rubatto et al*., 2009], pulsed crystallization which cannot be resolved by the 25 μm spot size of the SHRIMP-RG, or partial inheritance of radiogenic Pb from zircon cores, the former being our preferred model. Zircon rims and cores are distinguishable by their REE characteristics, but there is no correlation between zircon rim REE composition and age (see supplementary data).

[21] Leucosome SK 56 zircon rim ages range 28.5 to 15.5 Ma, with some discordance, and a poorly-defined cluster at 24.4 ± 0.7 Ma (n = 5, MSWD = 12) (Figure 5a). Zircon rim ages in sample SK 57, which cross-cuts sample SK 56, range 22.7-13.0 Ma, with most spot ages falling between 18–14 Ma (Figure 5b). In the aplite dyke SK 58, some rims of possible metamorphic origin (lacking oscillatory zoning, Th/U ratios ≤ 0.02) yield 33.1 ± 0.9 Ma (n = 4, MSWD = 2.7), while the rest of the dated zircon rims exhibit only weak oscillatory zoning and yield a spread of ages between 26.7-16.8 Ma (Th/U ratios ≥ 0.02) (Figure 5c). SK 60, the cordierite-bearing granite, yields zircon rim ages of 19.8-13.4 Ma, with a poorly-defined cluster at ca. 15.5 Ma (Figure 5d). SK 74 yielded few Miocene-aged concordant grains (Figure 5e).

3.1.3. Ti-in-Zircon Thermometry

[22] Zircon rim crystallization temperatures were determined from Ti-in-zircon thermometry measurements [*Watson et al*., 2006] also using the SHRIMP-RG at Stanford University (Supporting Information, Table S2). Ti measurements were made directly adjacent to U-Pb measurements, and CL images were used to ensure that the same chemical phase was sampled. Analytical procedures can be found in Appendix A. Ti-in-zircon thermometry requires assumptions about the activities of SiO_2 and TiO_2. Since our rocks are quartz-bearing, $a_{SiO2} = 1.0$. Igneous rocks typically have a_{TiO2} of 0.5-1.0 [*Watson and Harrison*, 2005], and since our leucogranite samples do not contain major Ti-bearing phases such as ilmenite or titanite, we assume $a_{TiO2} < 1.0$. As in our previous studies [e.g. *Kellett et al*., 2009], we have calculated temperatures using the revised calibration of *Ferry and Watson* [2007] and $a_{TiO2} = 0.5$ (likely maximum temperatures). Temperatures calculated for $a_{TiO2} = 0.7$ are also shown in Supporting Information, Table S2 for comparison, and are in general ~30 °C lower.

[23] The apparent Ti-in-zircon temperatures for Miocene zircon from all samples predominantly fall within the range of 660–810 °C, with the spread of crystallization T within most samples spanning that full range. Sample SK 57 has an apparent increasing zircon crystallization T during 18–14 Ma. Sample SK 58 also has an apparent slight increase in T during 27–17 Ma. The other samples show no clear relationship between zircon crystallization T and U-Pb age. In summary, zircon crystallization temperatures are 660–810 °C during the period 27–14 Ma.

3.2. Monazite

3.2.1. Sample Microstructure

[24] Monazite was dated *in situ* via LA-ICP-MS in polished thin section for three samples, SK 62, SK 65B and SK 67B to constrain the timing of peak T metamorphism and post-peak T shearing.

[25] SK 62 is a coarse-grained garnet-biotite-sillimanite gneiss (Figures 3d and 4c). Quartz microstructure is characterized by elongated ribbon grains surrounded by recrystallized grains indicating subgrain rotation recrystallisation (SGR). Recrystallized grains are about the same size or slightly larger than subgrains within the porphyroclastic ribbon grains. There are some micron-scale bulges along the grain boundaries indicating a retrograde overprint by bulging recrystallization. Feldspar contains deformation twins and myrmekite. Garnet grains are pervasively fractured, with fractures aligning with the gneissic fabric and not extending beyond garnet grain boundaries. Strain shadows around garnet contain biotite, quartz and sillimanite. Sillimanite occurs in fibrous mats and in shear bands. Monazite occurs included in garnet, mica, quartz and also at grain boundaries.

[26] SK 65B is a metapelitic mylonite gneiss containing biotite, plagioclase, sillimanite (both fibrous and prismatic), garnet, muscovite and tourmaline (Figures 3e and 4d). The mylonite fabric is very fine-grained, localized along quartz-mica-rich layers, and folded at mm-scale with NE vergence. Quartz deformation microstructure includes undulose extinction, SGR and grain boundary migration recrystallization. A

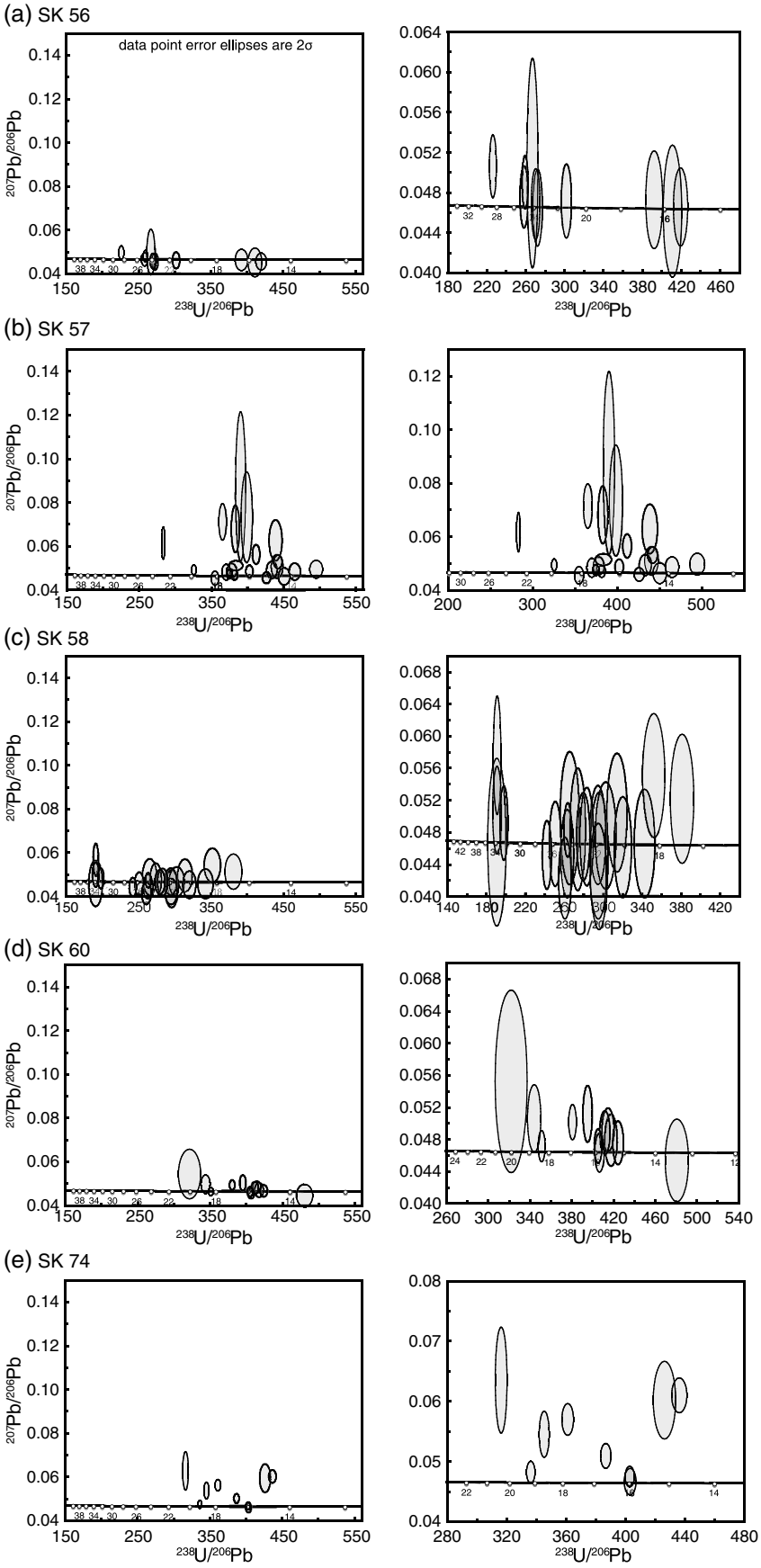

Figure 5. Zircon U-Pb geochronology displayed in Tera-Wasserburg plots. The data are plotted with a common scale bar in the left column for comparison, and expanded in the right column for clarity.

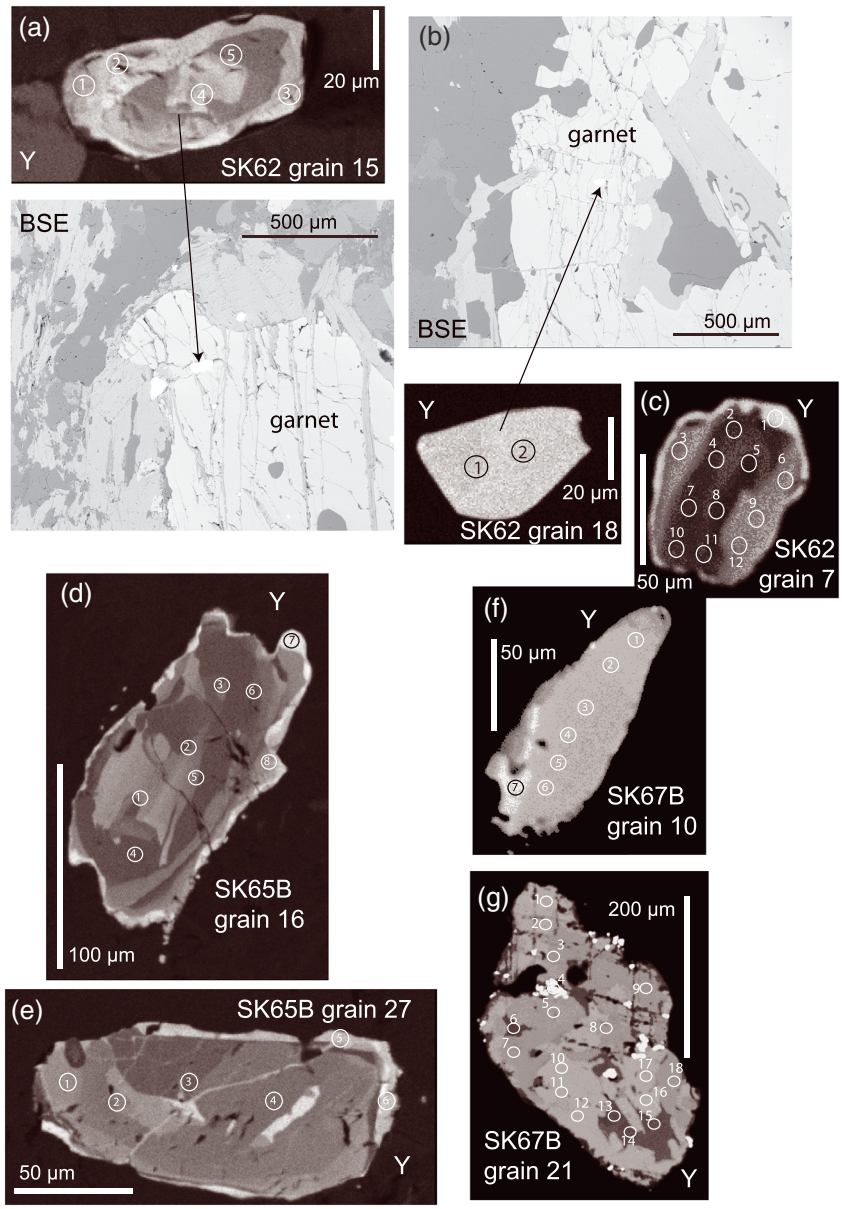

Figure 6. EMP mapping of monazite. BSE and Y maps are labeled accordingly, and numbered circles indicate laser ablation targets, and correspond to data in the Supporting Information, Tables S3 and A2. For Y maps, lighter colors signify relatively higher Y concentration. (a) and (b) are monazites included in garnet grains in SK62. While (a) is complexly-zoned, (b) is not. Neither exhibits the characteristic thin, high-Y rim observed in the matrix monazite from this sample (c) and SK65B (d, e). SK67B monazites are primarily small and lack zoning (e.g. (f)). However, one large grain (g) does show complex Y zoning.

weak S-C fabric is evident, recording top-to-the-NE sense of shear (Figure 4d). Monazite is situated primarily within the mylonitic matrix of this sample, with few grains included in feldspar.

[27] SK67B, a mylonitic augen gneiss, contains quartz, plagioclase, biotite and muscovite, with minor garnet, as well as abundant post-deformational tourmaline. A sample from the same outcrop also contains rutile rimmed by ilmenite. Mylonitization has greatly reduced grain size of quartz and feldspar due to SGR recrystallization, and ultramylonite is locally preserved. Feldspar porphyroclasts preserve myrmekite and microcline twinning. The mylonite fabric is locally folded at cm-scale with consistent NE vergence. S-type porphyroclasts of plagioclase and mica fish also preserve top-NE sense-of-shear. In this sample, monazite is located in mylonitic bands, at grain boundaries, and associated with mica-rich shear bands.

3.2.2. Quantitative and Qualitative Characterization of Monazite

[28] Back-scattered electron (BSE) and X-ray elemental maps of Y, La, Nd, Th and U in *in situ* monazite grains were collected to characterize elemental zoning using the JEOL 8200 electron microprobe (EMP) operated at Dalhousie University in Halifax, Canada (Figure 6). The maps were

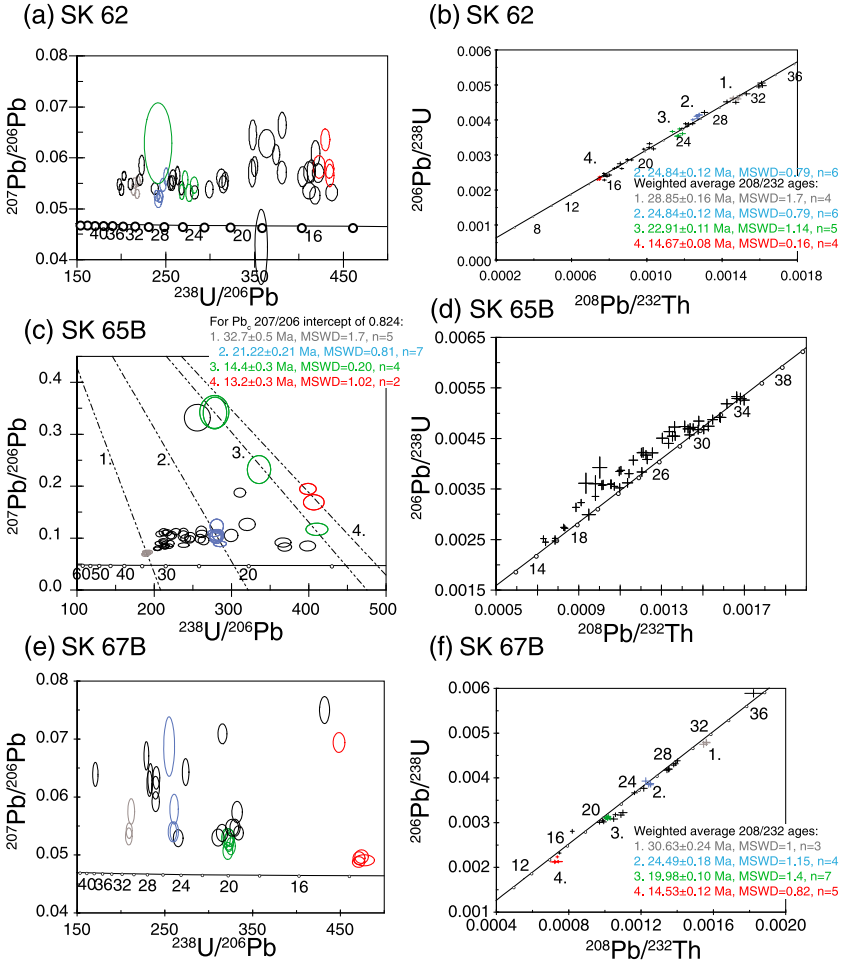

Figure 7. Monazite U-Th-Pb geochronology. Coloured data points indicate those analyses used to calculate the ages listed in figure.

used to guide laser ablation sites for quantitative trace element analysis and U-Th-Pb analysis [e.g. *Gibson et al.*, 2004]. Monazite grains in both SK62 and SK65B range in size from 20–150 µm in diameter, with the larger grains typically displaying complex chemical zoning, particularly in Y (Figure 6c, d, e). Matrix monazite grains are commonly rimmed by a high-Y domain compared to the cores. In contrast, monazite included in garnet locally displays complex zoning but overall lacks the thin high-Y rims of the matrix monazite (Figure 6a, b). SK67B monazite grains are primarily smaller than 20 µm in diameter, and lack resolvable elemental zoning (e.g. Figure 6f). However, few larger grains and particularly grain 22, which has a diameter of 400 µm, are zoned in Y, Th and U (Figure 6g).

[29] Age data for monazite were collected concurrently with quantitative trace element data at the University of California, Santa Barbara (UCSB) by splitting the stream of ablated material as it leaves the ablation chamber and directing it to both a Nu Plasma multi-collector ICP-MS for U-Th-Pb analysis and a Nu AttoM single-collector ICP-MS for trace element analysis [e.g. *Kylander-Clark et al.*, 2011]. The key advantage of this method is that trace element information and age information are measured from the same ablated material. A detailed description of the analytical conditions can be found in Appendix A of the supplementary material.

3.2.3. U-Th-Pb Geochronology Results

[30] U-Th-Pb ages of young (Tertiary) monazite can be challenging to interpret because of the difficulty in resolving contributions of non-radiogenic Pb (Pb_c), low abundances of radiogenic ^{207}Pb, and excess ^{206}Pb present as the decay product of unsupported ^{230}Th taken up during monazite crystallization [e.g. *Schärer*, 1984]. Tera-Wasserburg diagrams, ideal for visualizing young U-Pb ages, show that our monazite data are typically discordant. Since ^{206}Pb is in the denominator on both axes of these plots, unsupported ^{230}Th resulting in excess ^{206}Pb will skew data down and to the left of concordia [*Schärer*, 1984]. In addition, Pb_c will affect both the numerator and the denominator of the y-axis, and the denominator of the x-axis, skewing data up and to the left of concordia. By comparison, U-Th-Pb concordia plots, in which $^{206}Pb/^{238}U$ is plotted on the y-axis and $^{208}Pb/^{232}Th$ is plotted on the x-axis, should be favored for interpretation of low Pb/young monazite age data, because excess ^{206}Pb only affects values along the y-axis, driving data up from concordia (i.e. a single age population should form a vertical array of variable excess ^{206}Pb). In addition, because Th is more abundant than U in monazite (e.g. average Th/U = 7 in SK67B), radiogenic ^{208}Pb should largely swamp $^{208}Pb_c$, compared to radiogenic ^{206}Pb vs. $^{206}Pb_c$. For these reasons, we present both plots, and favor the weighted average Th-Pb ages, though we

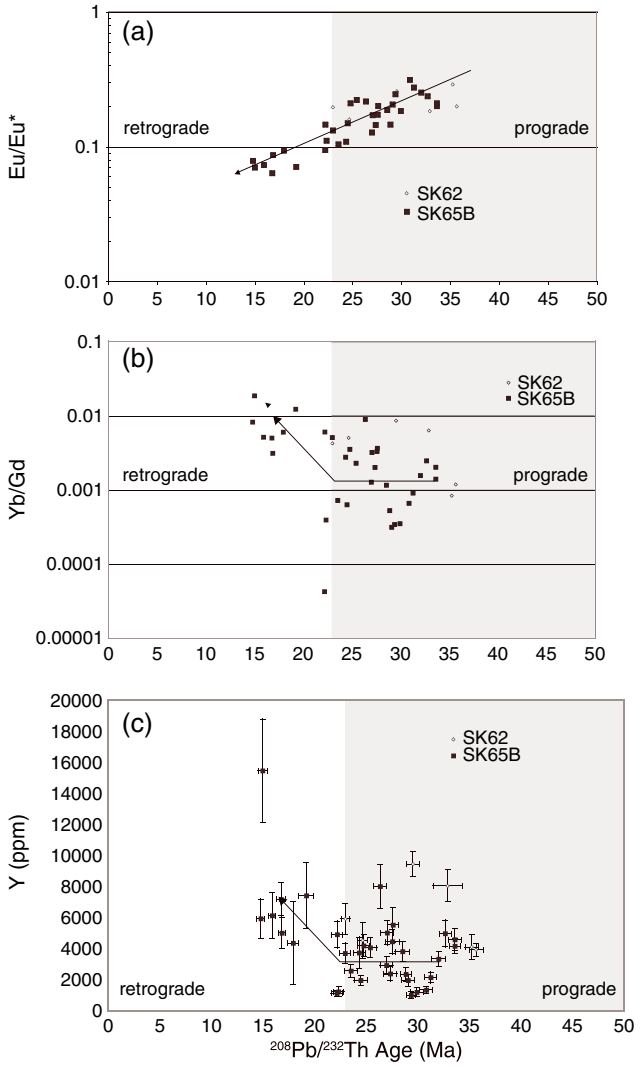

Figure 8. Plots of trace element data for monazite. Data are normalized to chondrite values of Anders and Grevesse [1989]. SK62 monazite shown in open diamonds is included in garnet, and defines the 'prograde' field (shaded in grey), while younger monazite from the matrix of SK65B defines the 'retrograde' field of monazite growth. (a) Eu/Eu* (defined in text) vs. ^{208}Pb/^{232}Th age (Ma), (b) Yb/Gd vs. ^{208}Pb/^{232}Th age (Ma), and (c) Y (ppm) vs. ^{208}Pb/^{232}Th age (Ma). Arrows indicate first-order prograde and retrograde trends of data only, and do not capture obvious complexities.

report U-Pb ages for comparison. For our U-Pb data, we use a Pb_c composition measured in feldspar to calculate approximate U-Pb ages.

[31] Sample SK 62 yields a spread in ages from ~32 to 14.6 Ma (Th-Pb). The Tera-Wasserburg diagram (Figure 7a) shows ages that are normally discordant, while the U-Th-Pb concordia plot (Figure 7b) shows the data to be slightly reversely discordant to concordant, indicating the presence of both excess ^{206}Pb and Pb_c. Thus, ^{208}Pb/^{232}Th weighted mean ages yield the best estimate of true age. Inherited cores are preserved in monazite grains that are included in garnet, and form a discordia line of Pb loss from ca. 450 Ma to the Miocene (not plotted, see Supporting Information, Table S3). The complex Y and age zoning in these monazites for both the inherited ages and later growth/recrystallization between ca. 35–24 Ma (^{208}Pb/^{232}Th ages) attest to a long history of monazite dissolution and growth/recrystallization. The youngest monazite included in garnet is 23.6 Ma. Weighted mean ^{208}Pb/^{232}Th ages suggest monazite growth in the sample occurred at 28.9 ± 0.2 Ma (MSWD = 1.7, n = 4), 24.8 ± 0.1 Ma (MSWD = 0.8, n = 6), 22.9 ± 0.1 Ma (MSWD = 1.1, n = 5) and 14.7 ± 0.1 Ma (MSWD = 0.2, n = 4).

[32] SK 65B (Figure 7c, d) contains a significant Pb_c component and tie-lines show that a Pb_c ^{207}Pb/^{206}Pb intercept of 0.836, measured in feldspar from this sample, is a good approximation of the Pb_c composition. The U-Th-Pb concordia plot shows the data to be slightly discordant. This sample yields the following ^{208}Pb/^{232}Th ages: earliest preserved monazite growth at 33.9 ± 0.3 Ma (MSWD = 2.0, n = 4), populations at 29.3 ± 0.5 Ma (MSWD = 3.3, n = 6), 27.3 ± 0.4 Ma (MSWD = 1.5, n = 5) and 24.6 ± 0.2 Ma (MSWD = 1.2, n = 5), as well as a spread of younger ages along concordia towards the youngest ages of 15.9 ± 0.2 (n = 2) and 14.9 ± 0.2 (n = 2) (Figure 7d). For this sample, we use Pb_c tie-lines to approximate U-Pb ages (Figure 7c). Using this technique the sample yields ages ranging from ~33 to 13 Ma. Earliest recorded monazite growth is at 32.7 ± 0.5 Ma (MSWD = 1.7, n = 5). Seven spot ages yield 21.2 ± 0.2 Ma (MSWD = 0.8), and the even spread of ages between 32.7 and 21.2 Ma appears to be a result of mixed sampling between these two age populations. Two groups of data provide estimates for latest monazite growth: 14.4 ± 0.3 Ma (MSWD = 0.2, n = 4) and 13.2 ± 0.3 Ma (n = 2). The ^{208}Pb/^{232}Th ages are used to plot against trace element composition below (section 4.2.4). There was no evidence for an inherited population in this sample.

[33] SK67B yields four distinct age populations (Figure 7e, f). The three older age groups correspond to relatively low Y content, while the youngest age group corresponds to relatively high Y content. Since the Pb_c component appears to be minor, and ages are near concordant to concordant in U-Th-Pb space, we report weighted mean ^{208}Pb/^{232}Th ages (Figure 7f). The oldest population recorded in this sample is 30.63 ± 0.24 Ma (MSWD = 1, n = 3). Weighted mean age populations are also present at 24.5 ± 0.2 Ma (MSWD = 1.2, n = 4), 20.0 ± 0.1 Ma (MSWD = 1.4, n = 7) and the youngest age group is at 14.5 ± 0.1 Ma (MSWD = 0.8, n = 5). There is no evidence for an inherited population in this sample.

3.2.4. Trace Element Evolution in Monazite

[34] It has been observed in previous studies [e.g. *Vance et al*., 2003; *Gibson et al*., 2004] that Y content changes in metamorphic rocks reflect changes in the Y budget of the rock due to growth or breakdown of garnet. Here we observe a complicated pattern of Y concentration with ^{208}Pb/^{232}Th age for monazite included in garnet (SK 62) and matrix monazite (SK 65B). Y content in prograde monazite (if we assume monazite included in garnet predates peak T metamorphism, shaded grey in Figure 8a-c) fluctuates from ~4000-5000 ppm at 33.9 ± 0.3 Ma to <2000 ppm at 29.3 ± 0.5 Ma back to ~4000 ppm at 27.3 ± 0.4 Ma during prograde growth, and then increases to 6000–8000 ppm during garnet breakdown post ca. 24 Ma. The trace element patterns of monazite exhibit the characteristic negative slopes and consistently negative Eu anomalies common to metamorphic monazite [e.g. *Spear and Pyle*, 2002]. In comparing trace element compositional

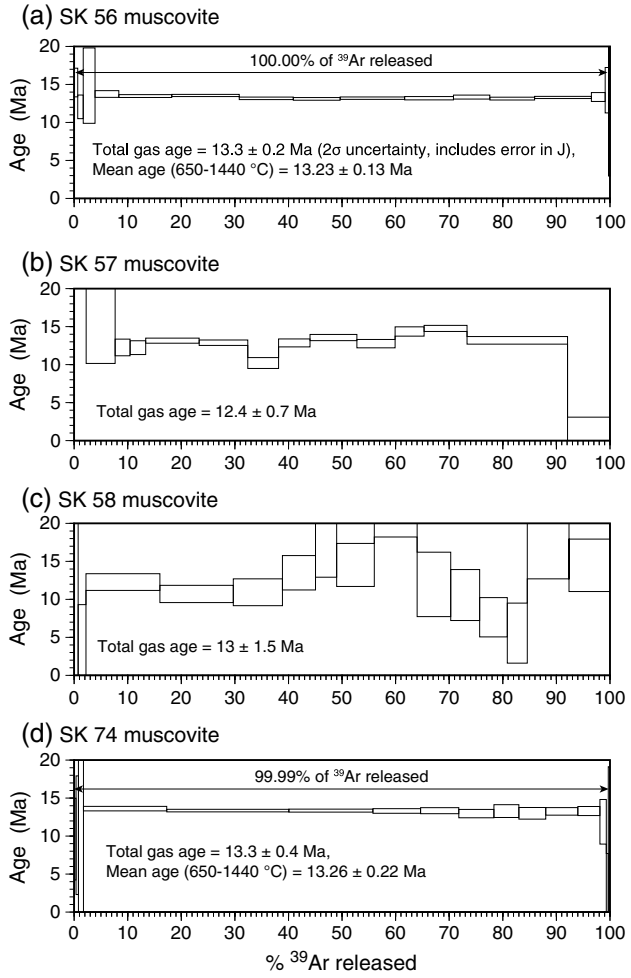

Figure 9. $^{40}Ar/^{39}Ar$ step heat profiles.

data with monazite $^{208}Pb/^{232}Th$ ages, some interesting trends are observed. The negative Eu anomaly Eu/Eu* (where Eu expected, or Eu* = Sm + ((Gd-Sm)/2), chondrite-normalized values) is more pronounced with decreasing isotopic age from ~0.4 at 35 Ma to ~0.06 at 15 Ma (Figure 8a), however there is no marked difference in trend between prograde and retrograde monazite. The slope of heavy rare earth elements (HREE), as defined by Yb/Gd, steepens with decreasing age from < 0.01 to > 0.01 (Figure 8b). More specifically, the log of Yb/Gd is correlated with Y content, and age, while the log of Eu/Eu* is broadly the inverse. *Rubatto et al*. [2012] suggest that decreases in Eu/Eu* in monazite may reflect increases in K-feldspar, while increases in HREE are indicative of garnet breakdown. These findings demonstrate that Y content in monazite in our samples is a sensitive monitor of changes in HREE and Eu availability during monazite growth.

[35] As for many other studies of metamorphic monazite [e.g. *Gibson et al*., 2004], monazite ages in our samples span a range of ages throughout the metamorphic history of the rock from inherited and prograde (preserved as inclusions in garnet) to retrograde (high-Y rims presumably grown during garnet and possibly xenotime breakdown). This age span is valuable for allowing us to track changes to the REE budget of the rock as a consequence of metamorphism [e.g. *Spear and Pyle*, 2002] and possibly deformation [*Lanzirotti and Hanson*, 1996]. In our samples, peak T is constrained by the ages of monazite included in garnet as ≤23.6 Ma, coinciding with partial melting conditions of the upper GHS during ~26-23 Ma [*Rubatto et al*., 2012]. Post-peak T breakdown of garnet, and concomitant release of HREEs is recorded by the increasing Yb/Gd slope in progressively younger monazite in the matrix compared to older monazite both included in garnet and in the matrix (Figure 8b), and an overall increase in Y content over the same time interval (Figure 8c).

3.3. Thermochronology

3.3.1. Muscovite $^{40}Ar/^{39}Ar$ Thermochronology

[36] The samples that were used for zircon U-Pb analysis were also separated for muscovite $^{40}Ar/^{39}Ar$ thermochronology. Bulk separates of muscovite from leucosome SK 56 and leucogranites SK 57, SK 58 and SK 74 were hand-picked for $^{40}Ar/^{39}Ar$ thermochronology (SK 60 was not analyzed for $^{40}Ar/^{39}Ar$ as it contains <5% very fine-grained muscovite). SK 56 muscovite grains are anhedral and associated with sillimanite in shear bands. In the leucogranites, muscovite is also anhedral, and grain size ranges from ~500 μm (SK 58 aplite) to 3–5 mm (SK 74). Muscovite defines a foliation in SK 56, and appears randomly oriented in the other samples.

[37] $^{40}Ar/^{39}Ar$ step heat thermochronology of muscovite separates was conducted at Dalhousie University, in Halifax, Canada using a Heine-based Ta double-vacuum furnace. Sample preparation, experimental procedures and analytical results are outlined in Appendix A of the supplementary data. All plateau ages are reported at the 2σ confidence level.

[38] Muscovite from SK 56 produced a well-defined plateau age of 13.23 ± 0.13 Ma (includes 100 % of ^{39}Ar released over 16 heating increments, MSWD = 0.51, probability = 0.94). The total gas age of the sample is 13.2 ± 0.3 Ma (Figure 9a). SK 57, the leucogranite that cross-cuts SK 56, did not yield a statistically-significant plateau, and produced a total gas age of 12.4 ± 0.7 Ma (Figure 9b). SK 58, the aplite dike, yielded a total gas age of 13.0 ± 1.5 Ma (Figure 9c). SK 74 yielded a well-defined plateau age of 13.26 ± 0.22 Ma (includes 99.99 % of ^{39}Ar released over 16 of 17 heating increments, MSWD = 0.34, probability = 0.99). The total gas age for the sample is 13.3 ± 0.4 Ma (Figure 9d).

[39] PT paths of the upper GHS in Sikkim indicate the gneisses experienced rapid, near-isothermal (~800 °C) decompression from >1 GPa to ~0.4 GPa, followed by cooling [*Neogi et al*., 1998; *Ganguly et al*., 2000]. Thus we infer that cooling of the leucogranites took place at pressures in the range of ≤0.4 GPa, which we use to estimate closure temperatures for Ar diffusion in muscovite. The presence of apparently magmatic cordierite in SK 60 is consistent with this inference (similar emplacement depths were calculated for cordierite-bearing leucogranites in similar structural position in the Everest region and Bhutan; e.g. *Streule et al*., 2010; *Kellett et al*., 2009; *Visoná et al*., 2012]. A comparison of zircon crystallization ages of 16–14 Ma at ~700 °C with an apatite fission track (AFT) age from another leucogranite (described below) of ~12 Ma at ~120 °C yields a minimum cooling rate over the time interval of interest of 145 °C/myr. Thus for our samples, with muscovite radii 100–500 μm, we estimate an approximate Ar closure temperature of 440–500 °C [*Harrison*

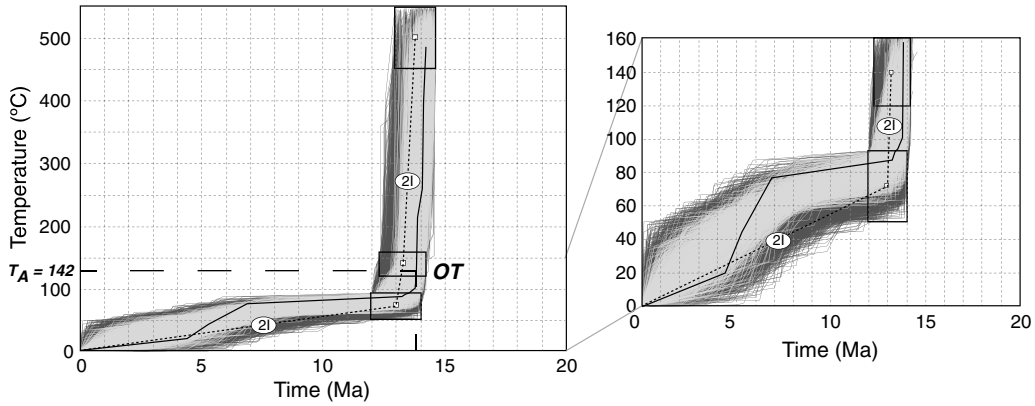

Figure 10. Representative HeFTy models for SK55. The black boxes represent time-temperature constraints. To prevent strong forcing of T-t paths, initial sizes of the boxes were set large and progressively reduced in order to optimize the search for good fits. Good fit solutions are represented by light grey paths and acceptable fit solutions by dark grey paths. The thick black line is the best fit T-t path. OT is the oldest track formed at T_A, the total annealing temperature. Using the Monte Carlo random search, each model run had 10,000 iterations, with episodic path segments and two half-segments evenly spaced between adjacent constraints. 2I indicates that the model has intermediate path segments and two half-segments evenly spaced between adjacent constraints.

et al., 2009]. Although grain size is significantly larger in SK 74 (1.5-2.5 mm radii), and thus we expect an even higher closure temperature for Ar in this sample, the plateau age is identical to that for the other samples which have finer-grained muscovite, providing further evidence that the cooling rate was rapid.

3.3.2. Low Temperature Thermochronology

[40] Apatite fission track and (U-Th)/He dating are well-established thermochronometric techniques that are widely employed in tectono-geomorphic studies to constrain the thermal history of the upper 5 km of the continental crust [e.g. *Farley*, 2002; *Donelick et al*., 2005; Reiners and Brandon, 2006]. Fission track thermochronology is based on the spontaneous fission decay of ^{238}U in uranium-bearing minerals which creates linear damage zones (fission tracks) in the crystal lattice. In apatite crystals, tracks can be retained at temperatures below about 120–150 °C, depending on the cooling rate and kinetic characteristics of the crystal [e.g. *Ketcham et al*., 1999]. (U-Th)/He dating is based on the decay of ^{235}U, ^{238}U, ^{232}Th (and ^{147}Sm) by α (^{4}He nucleus) emission. The ^{4}He is lost from apatite by thermally activated diffusion at temperatures above about 80 °C, and quantitatively retained below 40 °C [e.g. *Stockli et al*., 2000; *Wolf et al*., 1998].

3.3.2.1. Apatite Fission Track (AFT) Dating

[41] Four samples (SK69-SK72) were collected on the northeastern flank of the Thanggu valley, along a vertical profile spanning 650 m in elevation and two samples (SK55 and SK74) were collected in the uppermost footwall of the STDS, south of Lake Gurudongmar for AFT dating (Figure 1b). The analytical procedure, conducted at Dalhousie University, is described in the supplementary data. Samples SK69 to SK72 yielded ages between 6.50 ± 0.85 Ma and 7.61 ± 0.55 Ma (Supporting Information, Table S5). Sample SK74 did not yield sufficient apatite crystals to perform an analysis. Sample SK55 yielded a central age of 12.95 ± 0.69 Ma. Dpar values between 2.49 and 2.05 µm associated with relatively low standard deviations (Supporting Information, Table S5), indicate that these samples contain apatite crystals with similar annealing behavior. Importantly, all samples passed the χ^2 test, indicating that the single-grain ages are consistent with a common age for each sample.

[42] Samples along the vertical profile indicate similar ages (within 1σ error) with no systematic variation with elevation. This suggests that this crustal segment was rapidly cooled between 8–6 Ma from about 120 °C to the near surface temperatures. Lack of confined track lengths for these samples precludes further detailed interpretation.

[43] Twenty-eight confined track-lengths could be measured in sample SK55 with a mean track-length value of 13.77 ± 0.38 µm and a standard deviation of 1.99 µm (Supporting Information, Table S5). To reconstruct the T-t path of this sample, we have performed thermal modeling (see 3.3.2.3 Thermal modeling).

3.3.2.2. Apatite (U-Th)/He Dating (AHe)

[44] Five apatite aliquots from sample SK55 were processed for AHe dating (Supporting Information, Table S6). He measurements were conducted at Dalhousie University, while U, Th and Sm measurements were performed at ETH in Zurich, Switzerland. For a description of the methodology, see the supplementary data. The mean corrected age of the five grains is 15.18 ± 1.56 Ma, overlapping, within error, the AFT central age for this sample. However, grains SK55-4 and SK55-5 yielded ages significantly older than the central AFT age (20.20 and 17.12 Ma, respectively) and therefore have been discarded. The mean based on grains SK55-1 to 3 yields an age of 12.86 ± 0.77 Ma, making the AHe and AFT ages nearly identical.

3.3.2.3. Thermal Modeling

[45] We conducted a set of models based on the results obtained from AFT and AHe multi-thermochronometry performed on sample SK55 and muscovite ^{40}Ar/^{39}Ar results obtained for samples SK56, SK57 and SK58 located about 11 km west of SK55 in a similar structural position, i.e. in the immediate footwall of the STDS (Figures 1b and 10).

Thermal modeling was performed combining *c*-axis projected track lengths, single grain ages, and Dpars using the HeFTy program [Ketcham, 2005], implementing the annealing model of Ketcham *et al*. [2007]. Four constraints were used: 1) [500–440 °C] between [14.5-13 Ma] which corresponds to the age range of the oldest muscovite $^{40}Ar/^{39}Ar$ data, 2) [150–120 °C] between [14–12 Ma] as constrained by AFT data, 3) [90–50 °C] between [14–12 Ma] as constrained by AHe data and 4) [0–10 °C] at present according to the regional mean annual temperature at sea-level (25 °C), the atmospheric lapse rate (5.4 °C/km) and the present-day elevation of the sample.

[46] Out of 10,000 iterations, 2828 yielded acceptable fits and 978 good fits, reinforcing the strength of the thermal history documented by our data. The best-fit T-t paths indicate quasi-instantaneous cooling from 500 °C to 90 °C between 14 and 12 Ma after which cooling drastically slowed to about 7 °C/Ma (Figure 10). The best-fit T-t path suggests that the oldest fission track retained in the sample was formed at 13.8 Ma, when the sample cooled below a relatively high total annealing temperature of 142 °C, which is compatible with the fast cooling rates recorded for that time.

4. Discussion

4.1. Geochronology Interpretation

[47] PT paths and garnet growth modeling for the uppermost GHS in Sikkim indicate the gneisses experienced rapid near isothermal (at ~800 °C) decompression from >1 GPa to ~0.4 GPa within ~2-3 myr, followed by cooling during slower final exhumation [*Neogi et al*., 1998; *Ganguly et al*., 2000; *Rubatto et al*., 2012]. Our U-Th-Pb ages of prograde monazite included in garnet indicate that peak T metamorphism and consequently post-peak T decompression occurred after 23.6 Ma. U-Pb ages and Ti-in-zircon temperatures of zircon crystallization, and muscovite $^{40}Ar/^{39}Ar$, AFT and AHe cooling ages from leucogranites indicate that rapid cooling occurred during ca. 15–12 Ma (Figure 11a). If the leucogranitic melts had crystallized during the decompression of > 0.5 GPa, we would expect to observe an apparent decrease in Ti-in-zircon temperature during crystallization of ≥ 50 °C with time, due to the pressure dependence of uptake of Ti in zircon [*Watson et al*., 2006; *Ferry and Watson*, 2007; *Ferriss et al*., 2008; *Tailby et al*., 2011]. There is no clear pattern of decreasing apparent temperature except in SK 60, which displays a decrease of >100 °C at 16–15 Ma (excluding one outlier). It is possible that a pressure effect is not resolvable considering the overall spread in Ti-in-zircon temperatures of >100 °C without obvious trends in most samples. More likely, the leucogranites were all emplaced relatively late and at relatively shallow depths, as suggested for SK 60, which contains cordierite, and as suggested by the lack of well-developed deformation fabrics in all sampled magmatic bodies compared to the highly-deformed host gneiss.

[48] Considering the cooling history of the rocks and the relatively undeformed nature of the leucogranites, ductile deformation in the STDS footwall must have ended by about 13 Ma. Youngest monazite Th-Pb ages of ca. 14.5 Ma associated with shear bands also lead us to conclude that STDS-related shearing had ceased by ~13 Ma. Modeling of AFT and AHe data suggest that footwall rocks may have cooled down to as low as ~80 °C by 13–12 Ma, and that a period of slow cooling followed from that time until the rocks reached the surface (Figure 11). The coincidence of rapid cooling with latest possible ductile deformation of the STDS footwall demonstrates the central role of the STDS for cooling of hot metamorphic GHS rocks in Sikkim.

4.2. STDS Deformation and Footwall Exhumation

[49] Exhumation of GHS rocks in the footwall of the STDS occurred in three stages: 1. post-peak T, post-23.6 Ma rapid isothermal decompression; 2. 15–12 Ma rapid cooling with subdued decompression; 3. 12–0 Ma slow cooling and exhumation to surface. How does displacement on the STDS fit into this exhumation history?

[50] Low-angle normal-sense detachment systems in other tectonic environments such as metamorphic core complexes are also characterized by high-metamorphic grade footwalls, and the PT paths of those footwalls can, as in the eastern Himalaya, record large-magnitude isothermal decompression [e.g. *Teyssier and Whitney*, 2002; *Norlander et al*., 2002; *Whitney et al*., 2004]. In many cases, the detachment systems have been interpreted to be the principal exhumation structures [*Gessner et al*., 2001; Janák *et al*., 2001]. Although the tectonic regimes for such detachment systems are quite distinct from those forming the STDS (crustal extension vs. crustal shortening), the fault geometry and relative contrasts in T and peak metamorphic conditions are comparable. Numerical models of such detachment system geometry suggest that it is not possible to isothermally decompress footwall rocks by normal fault displacement in the absence of an additional heat source [*Fayon et al*., 2004]. *Fayon et al*. [2004] found that relatively steep fault angles (30°) are required to achieve significant decompression in the footwall of a detachment by normal slip on the structure. This results in a juxtaposition of hot footwall rocks against colder hanging wall rocks and thus cooling of the footwall during decompression. Lower-angle fault systems (10°) should not produce as rapid cooling of the footwall, but the low angle reduces the rate and total amount of throw, preventing large-magnitude decompression. Thus, depending on the angle of the fault system, either fast adiabatic decompression or slow cooling and decompression occur, but not isothermal or near-isothermal decompression. Since the orientation of the STDS at present may not be the same as when it was active during the Miocene, both cases can be compared. In the case of the STDS, which is part of a paired thrust-normal sense shear system, strain heating may, especially in the case of paired thrust and normal-sense shear zones, be a mechanism which produces heat and compresses isotherms to a higher degree than heat advection alone [*Nabelek et al*., 2010]. This would result in a steep apparent temperature gradient across a shear zone and a very fast cooling of material points moving across the isotherms. Other possible sources of heat that could explain the elevated geotherm in GHS rocks during the Miocene include: slab breakoff and upwelling of hot asthenosphere, which could have transferred a pulse of heat to the overlying crust [e.g. *King et al*., 2011]; vertical thinning for which there is evidence in the GHS and which would have the result of advecting hot, deep rocks towards the surface [e.g. *Law et al*., 2011; *Long*

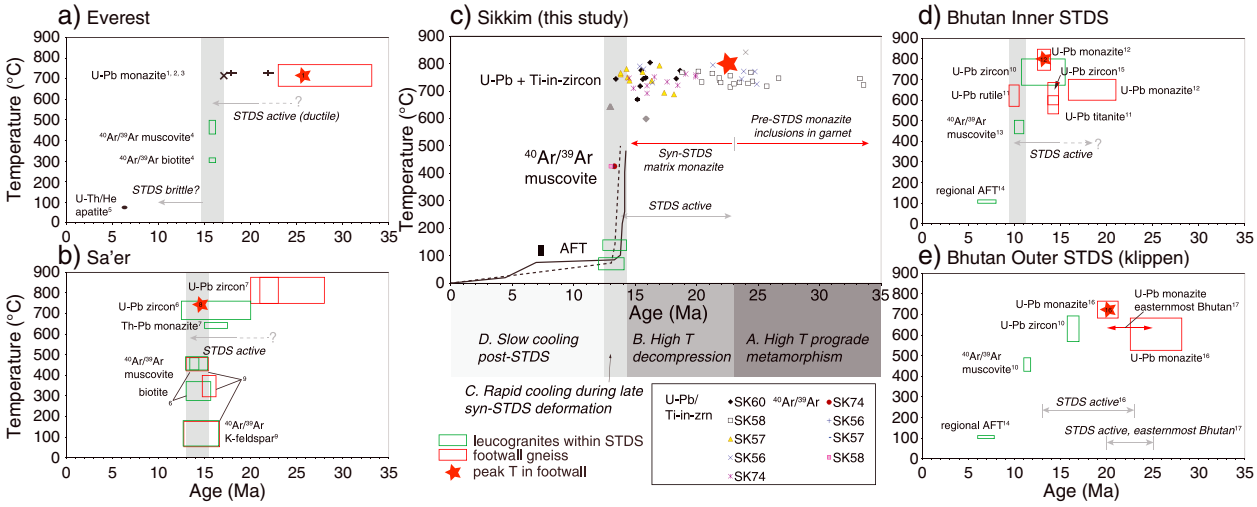

Figure 11. Compilations of geochronological data for the STDS from this study (c) and published work (a-b, d-e). Red stars denote estimated time and T of peak T metamorphism in the footwall. (a) Age data from the Everest section of the STDS, denoted by 1 in Figure 1a. M1 and M2 are metamorphic stages. (b) Age data from the Sa'er section of the STDS, denoted 2 in Figure 1a. (c) This study: U-Pb zircon ages + Ti-in-zircon temperatures ($a_{TiO2} = 0.5$) from leucogranite samples, Th-Pb monazite ages from metapelites (see text for comparison with U-Pb monazite ages), $^{40}Ar/^{39}Ar$ cooling ages, AFT data and AHe data. The red star denotes approximate peak T conditions for GHS granulites based on our monazite age data and PT work of *Neogi et al.* [1998], *Ganguly et al.* [2000] and *Rubatto et al.* [2012]. Outliers are in grey. For individual sample plots of U-Pb + Ti-in-zircon T-t plots, see Figure A6 in the supplementary data. (d) Age data from the inner STDS in Bhutan, denoted 3 in Fig. 1a. (e) Age data from the outer STDS in Bhutan, denoted 4 in Figure 1a. Note that for cases in which T conditions of monazite growth are not constrained, data are shown as lines instead of boxes or ellipses. 1. *Searle et al.*, 2003; 2. *Murphy and Harrison*, 1999; 3. *Simpson et al.*, 2000; 4. *Hodges et al.*, 1998; 5. *Hubbard and House*, 2000; 6. *Leloup et al.*, 2010; 7. *Kali et al.*, 2010; 8. *Cottle et al.*, 2009a; 9. *Hodges et al.*, 1994; 10. *Kellett et al.*, 2009; 11. *Warren et al.*, 2011b; 12. *Warren et al.*, 2011a; 13. *Maluski et al.*, 1988; 14. *Grujic et al.*, 2006; 15. *Grujic et al.*, 2011; 16. *Kellett et al.*, 2010; 17. *Chambers et al.*, 2011.

et al., 2011b], and; advection of partial melt magmas upwards through the GHS package towards the STDS, evidenced by the fact that the largest leucogranite plutons (e.g. Manaslu) occur at the top of the GHS section. The temporal link between rapid cooling and cessation of ductile motion on the STDS suggests that shear heating, vertical thinning and advection of heat by melt or release of latent heat by its crystallization may have all played a role. Without heat advection and strain heating, the isotherms, particularly in the upper crust, would rapidly relax to a normal geothermal gradient, radically slowing the cooling rate.

[51] Taking this into account, but considering as well that the STDS apparently asymptotes to a sub-horizontal detachment at the base of the upper crust/top of the mid-crust [e.g. *Nelson et al.*, 1996], we suggest that while slip on the STDS alone likely cannot account for rapid isothermal decompression of the footwall HT (and possibly HP → HT) rocks, the paired normal-thrust STDS-MCT system may have maintained high temperatures in the footwall during the later stages of exhumation by shear heating and vertical thinning. STDS deformation ceased around the time the rocks passed through muscovite $^{40}Ar/^{39}Ar$ closure and AFT PAZ temperatures, which coincides with a period of rapid cooling and slower decompression, and may reflect rapid relaxation of isotherms late- to post-deformation. This also supports the notion that shear heating and vertical thinning may have provided additional heat to the system. Both cooling and decompression slowed after displacement on the STDS ceased, as evidenced by AFT and AHe ages and thermal modeling. Thus, while the STDS could not have facilitated rapid isothermal decompression of HT rocks from the lower to mid-crust, it did facilitate continued isothermal decompression from mid-crust to the upper mid-crust, and the cessation of the STDS was important for their subsequent rapid cooling. This leads us to two major conclusions: 1. A mechanism is yet required to explain the rapid transport of HT rocks from the lower crust into the upper middle crust, and 2. The STDS facilitated Middle Miocene regional rapid cooling of mid- to lower crustal rocks in the eastern Himalaya, affecting both the heat budget and the rheology of the orogen.

4.3. Implications for Exhumation of High-Metamorphic Grade Rocks in the Eastern Himalaya

[52] It has been debated whether exhumation of the Ama Drime HP → HT rocks was primarily via slip on the orogen parallel [*Kali et al.*, 2010] or orogen-perpendicular [*Jessup et al.*, 2008; *Cottle et al.*, 2009a] normal fault systems. Considering the synchronicity in timing of the STDS and cooling history of footwall rocks in the Sa'er area with those in Sikkim [e.g. *Kali et al.*, 2010; *Leloup et al.*, 2010; Figure 11), and that most of the exhumation of these rocks

occurred as near-isothermal decompression [*Groppo et al*., 2007], we propose that as for Sikkim, the orogen-parallel STDS at Ama Drime may have been important for the latest stages of isothermal decompression in the presence of an additional heat source and subsequent cooling, that the later orogen-perpendicular structures were likely only important for upper crustal exhumation, and that a mechanism is yet required to explain the exhumation of HP → HT from the lower to mid-crust.

[53] *Warren et al*. [2011a] and *Grujic et al*. [2011] have proposed that insertion of a cold and stiff ramp indenter on the lower plate into weak and hot rocks in the upper plate could have forced lower-crustal rocks rapidly towards the surface in Bhutan. Geodynamic models of such a "plunger" in subduction systems have demonstrated that it can be an effective mechanism to exhume UHP rocks [e.g. *Warren et al*., 2008]. This concept is also supported by a numerical model of Himalayan-style continental collision [HT111 of *Jamieson et al*., 2006] in which cold, strong incoming lithosphere forms a rheological ramp on the basal detachment, and, similar to a rigid indenter, forces a dome of lower crustal rocks up and over the ramp. The material is ultimately extruded towards the surface between opposing-sense structures. PTt paths of some model nodes record peak pressures > 1.2 GPa and large-magnitude, high-temperature isothermal decompression, followed by rapid cooling + decompression [*Jamieson et al*., 2006]. In NW Bhutan, the granulite-facies rocks are bound by the STDS at the top and an out-of-sequence thrust at the base [*Grujic et al*., 2011; *Warren et al*., 2011a], which is consistent with HT111 model predictions. The timing of crustal melting in northern Sikkim [*Rubatto et al*., 2012] suggests two crustal levels; the higher structural levels reached melting and peak conditions later (26–23 Ma) than the lower structural levels (31–27 Ma). The boundary between the two crustal levels is near the latitude of township of Thangu (Figure 1b). However no thrust has been yet observed in the field. A detailed examination of age, deformation and metamorphism of GHS rocks between the MCT zone and the STDS should provide evidence or absence of evidence for a similar out-of-sequence thrust in Sikkim and elsewhere in the eastern Himalaya.

4.4. Timing of the South Tibetan Detachment System in the Eastern Himalaya

[54] The South Tibetan detachment system may be laterally continuous across most of the Himalayan orogen, but it was not active simultaneously along [*Godin et al*., 2006 and references therein) or across [*Kellett et al*., 2009] its strike (Figure 11). For example, in the Everest region, it appears that rapid cooling of the STDS footwall occurred at ~15 Ma [*Hodges et al*., 1998; *Murphy and Harrison*, 1999; *Hubbard and House*, 2000; *Simpson et al*., 2000; *Searle et al*., 2003; Figure 11a]. Rapid cooling of the hanging wall between ~350-130 °C occurred from 15.4 - 14.4 Ma [*Sakai et al*., 2005]. More recently, titanite U-Pb ages support cooling of the upper-most STDS footwall post ~13 Ma [*Cottle et al*., 2011], suggesting closer synchroneity with areas to the east. Between Everest and Sikkim, in the Sa'er area, latest ductile deformation on the STDS has been constrained to > 15 Ma, by considering that the youngest Th-Pb monazite ages in deformed and undeformed leucogranites correspond to the crystallization ages of the granites [*Leloup et al*., 2010]. However, if the youngest U-Pb zircon ages of the same samples are considered, for comparison with our zircon data, then the latest ductile deformation was after ca. 14.2 Ma and before ca 13.6 Ma (Figure 11b). Muscovite $^{40}Ar/^{39}Ar$ ages from the shear zone range between 15.2-13.6 Ma with a mean of 14.1 Ma [*Leloup et al*., 2010; Hodges *et al*., 1994; *Zhang and Guo*, 2007]. Latest brittle motion occurred between 13.6-11 Ma [*Leloup et al*., 2010]. East of Sikkim in NW Bhutan latest ductile deformation on the inner STDS has been constrained to during 11–10 Ma [*Maluski et al*., 1988; *Grujic et al*., 2006; *Kellett et al*., 2009; *Grujic et al*., 2011; *Warren et al*., 2011a; *Warren et al*., 2011b; Figure 11d]. This leaves a period of at least 1.6 myr and possibly more than 3 myr during which ductile motion on the STDS in the Sa'er-Sikkim-Yadong segment had ceased while it continued in NW Bhutan, east of the Yadong fault. Finally, the outer STDS in Bhutan, for which there is no late discrete low-angle normal-sense fault [*Kellett and Grujic*, 2012] does not record rapid cooling at all [*Grujic et al*., 2006; *Kellett et al*., 2009; 2010; *Chambers et al*., 2011] (Figure 11d).

[55] The leucogranites we dated from Sikkim are nearly undeformed, and thus constrain latest ductile motion to before ca. 13 Ma (the lack of young ages in aplite dyke SK58 is inconsistent with this, but aplites are emplaced and crystallize rapidly and in this case may not have yielded sufficient zircon overgrowths for age dating). This timing is coincident with the Sa'er STDS [*Leloup et al*., 2010], but not with the Bhutan inner STDS [*Kellett et al*., 2009] (Figure 11). There are two possible explanations for this. It may be that the Sa'er-Sikkim-Yadong segment of the STDS was a coherent structure, and disconnected from the NW Bhutan segment of the STDS after 13 Ma. This could have been accommodated by short-lived strike-slip tear faulting on the Nyonni Ri and Yadong fault systems, which seems consistent with available data [e.g. *Kali et al*., 2010; *Ratschbacher et al*., 2011]. Alternatively, if the inner STDS is a passive roof structure accommodating the extrusion of its footwall rocks, and coupled to the Kahktang thrust, then there need not have been any displacement of the Bhutan STDS hanging wall relative to the Sikkim STDS hanging wall, only relative motion of the footwalls. That scenario requires either no out-of-sequence thrust in East Nepal-Sikkim, or one with different timing of displacement than that in Bhutan. Tectonic discontinuities identified in GHS rocks in Bhutan [*Warren et al*., 2011a, 2011b] and Sikkim [*Rubatto et al*., 2012] although of different ages support the latter possibility. This again points to the need for a detailed study of GHS rocks between the MCT zone and the STDS in Sikkim and eastern Nepal in order to reconcile the apparently different models of exhumation of the Himalayan lower crust.

5. Conclusions

[56] This geo- and thermochronological study combined with published thermobarometric data on the footwall rocks of the South Tibetan detachment system in northern Sikkim indicate a sequence of four stages of PT evolution:

[57] 1. High temperature conditions, partial melting, and deformation in the footwall after 23.6 Ma;

[58] 2. Isothermal decompression from >1 GPa to ~0.4 GPa during ca. 2 myr;

[59] 3. Rapid cooling from ~700 to ~80 °C at ~155 °C/Ma between ~15-12 Ma;

[60] 4. Final slow cooling to the surface at ~6.5-7 °C/Ma since ~12 Ma.

[61] These data further indicate that the ductile motion along the STDS in the Sa'er-Sikkim-Yadong segment occurred between 23–13 Ma, and ceased about 2 Ma earlier than in the Bhutan Himalaya. Finally, we have demonstrated that the South Tibetan detachment system facilitated mid-crustal exhumation and rapid cooling of metamorphic rocks in the eastern Himalaya, but cannot be invoked to explain isothermal exhumation of high temperature and high pressure → high temperature rocks from lower crustal depths.

[62] **Acknowledgments.** We are grateful to Abhijit Chowdhury and our Sikkimese and Bengali guides and drivers for field assistance. We also thank Keith Taylor, Joe Wooden, Konstanze Stübner, Matthew Kliffer, Kyle Landry and Maria Giuditta Fellin for laboratory assistance. This work was supported by NSERC Discovery grants to D. Grujic and I. Coutand, NSF-EAR grant 1119380 to J. Cottle and D. Kellett, and a Fulbright Foundation Research Grant and France-Stanford Center Fellowship to I. Coutand. We thank An Yin and Tom Argles for constructive and critical reviews which improved the manuscript. We also thank Paul Kapp and Todd Ehlers for editorial handling. This manuscript is Geological Survey of Canada contribution #20120287.

References

Acton, C. E., K. Priestley, S. Mitra, and V. K. Gaur (2011), Crustal structure of the Darjeeling-Sikkim Himalaya and southern Tibet, *Geophys. J. Int.*, *184*, doi:10.1111/j.1365-246X.2010.04868.x.

Alsdorf, D., Y. Makovsky, W. Zhao, L. Brown, K. D. Nelson, S. Klemperer, M. Hauck, A. Ross, M. Cogan, M. Clark, J. Che, and J. Kuo (1998), INDEPTH (International Deep Profiling of Tibet and the Himalaya) multichannel seismic reflection data: Description and availability, *J. Geophys. Res.*, *103*, 26993–26999.

Anders, E. and N. Grevesse (1989), Abundances of the elements: Meteoritic and solar, *Geochim. Cosmochim. Acta*, *53*, 197–214.

Bhattacharyya, K. and G. Mitra (2009), A new kinematic evolutionary model for the growth of a duplex-an example from the Rangit duplex, Sikkim Himalaya, India, *Gondwana Res.*, *16*, 697–715.

Bhattacharyya, K. and G. Mitra (2011), Strain softening along the MCT zone from the Sikkim Himalaya: Relative roles of Quartz and Micas, *J. Struct. Geol.*, *33*, 1105–1121.

Borghi, A., D. Castelli, B. Lombardo, and D. Visonà (2003), Thermal and baric evolution of garnet granulites from the Kharta region of S Tibet, E Himalaya, *Eur. J. Mineral.*, *15*, 401–418.

Burchfiel, B. C. and L. H. Royden (1985), North-south extension within the convergent Himalayan region, *Geology*, *13*, 679–682.

Burchfiel, B. C., Z. Chen, K. V. Hodges, Y. Liu, L. H. Royden, C. Deng, and J. Xu (1992), The South Tibetan Detachment System, Himalayan Orogen: Extension Contemporaneous with and Parallel to Shortening in a Collisional Mountain Belt, *Geol. Soc. Am. 269*, 41.

Burg, J. P. and G. M. Chen (1984), Tectonics and structural zonation of southern Tibet, China, *Nature*, *311*, 219–223.

Burg, J. P., M. Brunel, D. Gapais, G. M. Chen, and G. H. Lui (1984), Deformation of leucogranites of the crystalline Main Central Sheet in southern Tibet (China), *J. Struct. Geol.*, *6*, 535–542.

Catlos, E. J., T. M. Harrison, C. E. Manning, M. Grove, S. M. Rai, M. S. Hubbard, and B. N Upreti (2002), Records of the evolution of the Himalayan orogen from in situ Th-Pb ion microprobe dating of monazite: Eastern Nepal and western Garhwal, *J. Asian Earth Sci.*, *20*, 459–479.

Catlos, E. J., C. S. Dubey, T. M. Harrison, and M. A. Edwards (2004), Late Miocene movement within the Himalayan Main Central Thrust shear zone, Sikkim, north-east India, *J. Metamorph. Geol.*, *22*, 207–226.

Chakungal, J., J. Dostal, D. Grujic, S. Duchêne, and K. S. Ghalley (2010), Provenance of the Greater Himalayan sequence: Evidence from mafic granulites and amphibolites in NW Bhutan, *Tectonophysics*, *480*, 198–212.

Chambers, J., R. Parrish, T. Argles, and N. Harris (2011), A short duration pulse of ductile normal shear on the outer South Tibetan detachment in Bhutan: Alternating channel flow and critical taper mechanics of the eastern Himalaya, *Tectonics*, *30*, doi:10.1029/2010TC002784.

Corrie, S. L., M. J. Kohn, and J. D. Vervoort (2010), Young eclogite from the Greater Himalayan Sequence, Arun Valley, eastern Nepal: PTt path and tectonic implications, *Earth Planet. Sci. Lett.*, *289*, 406–416.

Corrie, S.L., M.J. Kohn, N. McQuarrie, and S.P. Long (2012), Flattening the Bhutan Himalaya, *Earth Planet. Sci. Lett.*, *349–350*, 67–74.

Cottle, J. M., M. J. Jessup, D. L. Newell, M. S. A. Horstwood, S. R. Noble, R. R. Parrish, D. J. Waters, and M. P. Searle (2009a), Geochronology of granulitized eclogite from the Ama Drime Massif: Implications for the tectonic evolution of the South Tibetan Himalaya, *Tectonics*, *28*, doi:10.1029/2008TC002256.

Cottle, J. M., M. P. Searle, M. S. A. Horstwood, and D. J. Waters (2009b), Timing of midcrustal metamorphism, melting and deformation in the Mount Everest region of Southern Tibet revealed by U (−Th)–Pb geochronology, *J. Geol.*, *117*, 643–664.

Cottle, J. M., D. J. Waters, D. Riley, O. Beyssac, and M. J. Jessup (2011), Metamorphic history of the South Tibetan Detachment System, Mt. Everest region, revealed by RSCM thermometry and phase equilibria modeling, *J. Metamorph. Geol.*, *29*, 561–582.

Dasgupta, S., J. Ganguly, and S. Neogi (2004), Inverted metamorphic sequence in the Sikkim Himalayas: crystallization history, P–T gradient and implications, *J. Metamorph. Geol.*, *22*, 395–412.

DeCelles, P. G., G. E. Gehrels, Y. Najman, A. J. Martin, A. Carter, and E. Garzanti (2004), Detrital geochronology and geochemistry of Cretaceous-Early Miocene strata of Nepal: implications for timing and diachroneity of initial Himalayan orogenesis, *Earth Planet. Sci. Lett.*, *227*, 313–330.

Donelick, R. A., P. B. O'Sullivan, and R. A. Ketcham (2005), Apatite fission-track analysis, in Low-Temperature Thermochronology: Techniques, Interpretations, and Applications, Rev. Mineral. Geochem., vol. *58*, edited by P. W. Reiners and T. A. Ehlers, pp. 49–94, Mineral. Soc. of Am., Washington, DC.

Edwards, M. A., E. J. Catlos, T. M. Harrison, and C. S. Dubey (2002), We seek him now, we sought him then: 70 years of constraints on the STDS in Sikkim. 17th Himalaya-Karakoram-Tibet Workshop, Sikkim, India, *J. Asian Earth Sci.*, *20* (Suppl. 1), 11–12.

England, P. and P. Molnar (1990), Surface uplift, uplift of rocks, and exhumation of rocks, *Geology*, *18*, 1173–1177.

Ernst, W.G. (2001), Subduction, ultrahigh-pressure metamorphism, and regurgitation of buoyant crustal slices; implications for arcs and continental growth, processes and consequences of deep subduction, *Phys. Earth Planet. Inter.*, *127*, 253–275.

Farley, K. A. (2002), (U-Th)/He dating: techniques, calibrations, and applications, *Rev. Mineral. Geochem.*, *47*, 819–844, doi:10.2138/rmg.2002.47.18.

Farley, K., R. Wolf, and L. Silver (1996), The effects of long alpha-stopping distances on (U-Th)/He ages, *Geochim. Cosmochim. Acta*, *60*, 4223–4229.

Fayon, A. K., D. L. Whitney, and C. Teyssier (2004), Exhumation of orogenic crust: Diapiric ascent versus low-angle normal faulting, *Gneiss Domes and Orogeny*, 129–139.

Ferriss, E. D. A., E. J. Essene, and U. Becker (2008), Computational study of the effect of pressure on the Ti-in-zircon geothermometer, *Eur. J. Mineral.*, *20*, 745–755.

Ferry, J. M. and E. B. Watson (2007), New thermodynamic models and revised calibrations for the Ti-in-zircon and Zr-in-rutile thermometers, *Contrib. Mineral. Petrol.*, *154*, 429–437.

Ganguly, J., S. Dasgupta, W. Cheng, and S. Neogi (2000), Exhumation history of a section of the Sikkim Himalayas, India: records in the metamorphic mineral equilibria and compositional zoning of garnet, *Earth Planet. Sci. Lett.*, *183*, 471–486.

Gansser, A. (1964), Geology of the Himalayas, Interscience Publishers London, New York, Sydney, 289 p.

Gansser, A. (1983), Geology of the Bhutan Himalaya, Birkhčauser Verlag, Basel Switzerland and Boston, 181 p.

Gessner, K., U. Ring, C. Johnson, R. Hetzel, C. W. Passchier, and T. Güngör (2001), An active bivergent rolling-hinge detachment system: Central Menderes metamorphic core complex in western Turkey, *Geology*, *29*, 611–614.

Gibson, H. D., S. D. Carr, R. L. Brown, and M. A. Hamilton (2004), Correlations between chemical and age domains in monazite and metamorphic reactions involving major politic phases: an integration of ID-TIMS and SHRIMP geochronology with Y-Th-U X-ray mapping, *Chem. Geol.*, *211*, 237–260.

Godin, L., R. R. Parrish, R. L. Brown, and K. V. Hodges (2001), Crustal thickening leading to exhumation of the Himalayan metamorphic core of central Nepal: Insight from U-Pb geochronology and $^{40}Ar/^{39}Ar$ thermochronology, *Tectonics*, *20*, 729–747.

Godin, L., D. Grujic, R. Law, and M. P. Searle (2006), Crustal flow, extrusion, and exhumation in continental collision zones: An introduction, in Channel Flows, Ductile Extrusion and Exhumation in Continental Collision Zones, edited by R. D. Law, M. P. Searle, and L. Godin, *Geol. Soc. Spec. Publ.*, *268*, 1–23, doi:10.1144/GSL.SP.2006.268.01.01.

Gong, J., J. Jianqing, B. Han, J. Chen, D. Sun, B. Li, J. Zhou, J. Tu, and D. Zhong (2011), Early subduction-exhumation and late channel flow

of the Greater Himalayan Sequence: implications from the Yadong section in the eastern Himalaya, *Int. Geol. Rev.*, doi:10.1080/00206814.2011.626604.

Goscombe, B., and M. Hand (2000), Contrasting P-T paths in the eastern Himalaya, Nepal: Inverted isograds in a paired metamorphic mountain belt, *J. Petrol.*, *41*, 1673–1719.

Goscombe, B., D. Gray, and M. Hand (2006), Crustal architecture of the Himalayan metamorphic front in eastern Nepal, *Gondwana Res.*, *10*, 232–255.

Green, O. R., M. P. Searle, R. I. Corfield, and R. M. Corfield (2008), Cretaceous-Tertiary carbonate platform evolution and the age of the India-Asia collision along the Ladakh Himalaya (Northwest India), *J. Geol.*, *116*, 331–353.

Groppo, C., B. Lombardo, F. Rolfo, and P. Pertusati (2007), Clockwise exhumation path of granulitized eclogites from the Ama Drime range (Eastern Himalayas), *J. Metamorph. Geol.*, *25*, 51–75.

Grujic, D., I Coutand, B. Bookhagen, S. Bonnet, A. Blythe, and C. Duncan (2006), Climatic forcing of erosion, landscape, and tectonics in the Bhutan Himalayas, *Geology*, *34*, 801–804.

Grujic, D., C. J. Warren, and J. L. Wooden (2011), Rapid synconvergent exhumation of Miocene-aged lower orogenic crust in the eastern Himalaya, *Lithosphere*, *3*, 346–366.

Harris, N. B. W., M. Caddick, J. Kosler, S. Goswami, D. Vance, and A. G. Tindle (2004), The pressure–temperature–time path of migmatites from the Sikkim Himalaya, *J. Metamorph. Geol.*, *22*, 249–264.

Harrison, T. M., F. J. Ryerson, P. Le Fort, A. Yin, O.M. Lovera and E. J. Catlos (1997), A Late Miocene-Pliocene origin for the Central Himalaya inverted metamorphism, *Earth Planet. Sci. Lett.*, *146*, E1-E7.

Harrison, T. M., J. Célérier, A. B. Aikman, J. Hermann, and M. T. Heizler (2009), Diffusion of ^{40}Ar in muscovite, *Geochim. Cosmochim. Acta*, *73*, 1039–1051.

Hauck, M. L., K. D. Nelson, L. D. Brown, W. Zhao, and A. R. Ross (1998), Crustal structure of the Himalayan orogen at 90° east longitude from Project INDEPTH deep reflection profiles, *Tectonics*, *17*, 481–500.

Hébert, R., R. Bezard, C. Guilmette, J. Dostal, C.S. Wang, Z.F. Liu (2012), The Indus-Yarlung Zangbo ophiolites from Nanga Parbat to Namche Barwa syntaxes, southern Tibet: First synthesis of petrology, geochemistry, and geochronology with incidences on geodynamic reconstructions of Neo-Tethys, *Gondwana Res.*, *22*, 377–397.

Hetényi, G., Cattin, R., Nrune, F., Bollinger, L., Vergne, J., Nábelek, J. L., and Diament, M. (2007), Density distribution of the Indian plate beneath the Tibetan plateau: Geophysical and petrological constraints on the kinetics of lower-crustal eclogitization, *Earth Planet. Sci. Lett.*, *264*, 226–244.

Hodges, K. V., W. E. Eames, W. Olszewski, B.C. Burchfiel, L.H. Royden, and Z. Chen (1994), Thermobarometric and ^{40}Ar/^{39}Ar geochronologic constraints on Eohimalayan metamorphism in the Dinggyê area, southern Tibet, *Contrib. Mineral. Petrol.*, *117*, 151–163.

Hodges, K. V., R. R. Parrish, and M. P. Searle (1996), Tectonic evolution of the central Annapurna range, Nepalese Himalayas, *Tectonics*, *15*, 1264–1291.

Hodges, K.V., S. Bowring, K. Davidek, D. Hawkins, and M. Krol (1998), Evidence for rapid displacement on Himalayan normal faults and the importance of tectonic denudation in the evolution of mountain ranges, *Geology*, *26*, 483–486.

Hubbard, M. S., and M. House (2000), Low temperature dating of high mountain rocks: (U-Th)/He ages from Higher Himalaya samples, Eastern Nepal (Abtract), in 15th Himalaya-Karakoram-Tibet Workshop, Chengdu, pp. 16–17, Earth Science Frontiers, Beijing.

Jamieson, R. A., C. Beaumont, S. Medvedev, and M.H. Nguyen (2004), Crustal channel flows: 2. Numerical models with implications for metamorphism in the Himalayan-Tibetan orogen, *J. Geophys. Res.*, doi:10.1029/2003JB002811.

Jamieson, R. A., C. Beaumont, M.H. Nguyen, and D. Grujic (2006), Provenance of the Greater Himalayan Sequence and associated rocks: Predictions of channel flow models, in Channel Flows, Ductile Extrusion and Exhumation in Continental Collision Zones, edited by R. D. Law, M. P. Searle, and L. Godin, *Geol. Soc. Spec. Publ.*, *268*, 165–182, doi:10.1144/GSL.SP.2006.268.01.07.

Janák, M., D. Plašienka, M. Frey, M. Cosca, S. Schmidt, B. Lupták, and Š. Méres (2001), Cretaceous evolution of a metamorphic core complex, the Veporic unit, Western Carpathians (Slovakia): P–T conditions and in situ ^{40}Ar/^{39}Ar UV laser probe dating of metapelites, *J. Metamorph. Geol.*, *19*, 197–216.

Jarvis, A., H. I. Reuter, A. Nelson, and E. Guevara (2008), Hole filled seamless SRTM data V4, International Centre for Tropical Agriculture (CIAT), available from http://srtm.csi.cgiar.org.

Jessup, M. J., D. L. Newell, J. M. Cottle, A. L. Berger, and J. A. Spotila (2008), Orogen-parallel extension and exhumation enhanced by denudation in the trans-Himalayan Arun River gorge, Ama Drime Massif, Tibet-Nepal, *Geology*, *36*, 587–590.

Kali, E., P. H. Leloup, N. Arnaud, G. Mahéo, D. Liu, E. Boutonnet, J. Van der Woerd, X. Liu, J. Liu-Zeng, and H. Li (2010), Exhumation history of the deepest central Himalayan rocks, Ama Drime range: Key pressure-temperature-deformation-time constraints on orogenic models, *Tectonics*, *29*, TC2014, doi:10.1029/2009TC002551.

Kellett, D. A., and D. Grujic (2012), New insight into the South Tibetan detachment system: Not a single progressive deformation, *Tectonics*, *31*, doi: 10.1029/2011TC002957.

Kellett, D. A., D. Grujic, and S. Erdmann (2009), Miocene structural reorganization of the South Tibetan detachment, eastern Himalaya: Implications for continental collision, *Lithosphere*, *1*, 259–281, doi:10.1130/L56.1.

Kellett, D. A., D. Grujic, C. Warren, J. Cottle, R. Jamieson, and T. Tenzin (2010), Metamorphic history of a syn-convergent orogen-parallel detachment: The South Tibetan detachment system, Bhutan Himalaya, *J. Metamorph. Geol.*, *28*, 785–808.

Ketcham, R. A. (2005), Forward and inverse modeling of low-temperature thermochronometry data, *Rev. Mineral. Geochem.*, *58*, 275–314.

Ketcham, R. A., R. A. Donelick, and W. D. Carlson (1999), Variability of apatite fission-track annealing kinetics; III, Extrapolation to geological time scales, *Am. Mineral.*, *84*, 1235–1255.

Ketcham, R. A., A. Carter, R. A. Donelick, J. Barbarand, and A. J. Hurford (2007), Improved modeling of fission-track annealing in apatite, *Am. Mineral.*, *92*, 799–810.

King, J., N. Harris, T. Argles, R. Parrish, and Z. Hongfei (2011), Contribution of crustal anatexis to the tectonic evolution of Indian crust beneath southern Tibet, *Geological Society of America Bulletin*, *123*, 218–239.

Kylander-Clark, A., B. R. Hacker, and A. Ginsburg (2011), High-pressure tectonism: insights from laser ablation split-stream (LASS) petrochronology, 2011 GSA Annual Meeting in Minneapolis.

Lanzirotti, A. and G. N. Hanson (1996), Geochronology and geochemistry of multiple generations of monazite from the Wepawaug Schist, Connecticut, USA: implications for monazite stability in metamorphic rocks, *Contrib. Mineral. Petrol.*, *125*, 332–340.

Larson, K. P., L. Godin, and R. A. Price (2010), Relationships between displacement and distortion in orogens: Linking the Himalayan foreland and hinterland in central Nepal, *Bull. Geol. Soc. Am.*, *122*, 1116–1134.

Lavé, J., and J.P. Avouac (2000), Active folding of fluvial terraces across the Siwaliks Hills, Himalayas of central Nepal, *J. Geophys. Res.*, doi:10.1029/1999JB900292.

Law, R. D., M. J. Jessup, M. P. Searle, M. K. Francsis, D. J. Waters, and J. M. Cottle (2011), Telescoping of isotherms beneath the South Tibetan Detachment System, Mount Everest Massif, *J. Struct. Geol.*, *33*, 1569–1594.

Le Fort, P. (1975), Himalayas: The collided range. Present knowledge of the continental arc, *Am. J. Sci.*, *275-A*, 1–44.

Lee, J., B. R. Hacker, W. S. Dinklage, Y. Wang, P. Gans, A. Calvert, J. L. Wan, W. Chen, A. E. Blythe, and W. McClelland (2000), Evolution of the Kangmar Dome, southern Tibet: Structural, petrologic, and thermochronologic constraints, *Tectonics*, *19*, 872–895.

Leloup, P. H., G. Mahéo, N. Arnaud, E. Kali, E. Boutonnet, D. Lui, L. Xiaohan, and L. Haibling (2010), The South Tibet detachment shear zone in the Dinggye area. Time constraints on extrusion models of the Himalayas, *Earth Planet. Sci. Lett.*, *292*, 1–16.

Long, S., N. McQuarrie, T. Tobgay, C. Rose, G. Gehrels, and D. Grujic (2011a) Tectonostratigraphy of the Lesser Himalaya of Bhutan: Implications for the along-strike stratigraphic continuity of the northern Indian margin, *Geol. Soc. Am. Bull.*, doi:10.1130/B30202.1.

Long, S., N. McQuarrie, T. Tobgay and J. Hawthorne (2011b) Quantifying internal strain and deformation temperature in the eastern Himalaya, Bhutan: Implications for the evolution of strain in thrust sheets, *J. Struct. Geol.*, doi:10.1016/j.jsg.2010.12.011.

Maluski, H., P. Matte, M. Brunel, and X. Xiao (1988), Argon 39-argon 40 dating of metamorphic and plutonic events in the north and high Himalaya belts (southern Tibet-China), *Tectonics*, *7*, doi: 10.1029/TC007i002p00299.

Mitra, S., K. Priestley, A.K. Bhattacharyya, and V.K. Gaur (2005), Crustal structure and earthquake focal depths beneath northeastern India and southern Tibet, *Geophys. J. Int.*, *160*, doi:10.1111/j.1365-246X.2004.02470.x.

Mukul, M. (2000), The geometry and kinematics of the Main Boundary Thrust and related neotectonics in the Darjiling Himalayan fold-and-thrust belt, West Bengal, India, *J. Struct. Geol.*, *22*, 1261–1283.

Murphy, M.A. and T.M. Harrison (1999), Relationship between leucogranites and the Qomolangma detachment in the Rongbuk Valley, south Tibet, *Geology*, *27*, 831–834.

Nabelek, P. I., A. G. Whittington, and A. M. Hofmeister (2010), Strain heating as a mechanism for partial melting and ultrahigh temperature metamorphism in convergent orogens: Implications of temperature-dependent thermal diffusivity and rheology, *J. Geophys. Res.*, *115*, doi:10.1029/2010JB007727.

Nelson, K. D., W. Zhao, L. Brown, J. Kuo, J. Che, X. Liu, S. Klemperer, Y. Makovsky, R. Meissner, and J. Mechie (1996), Partially molten middle crust beneath southern Tibet: Synthesis of project INDEPTH results, *Science*, *274*, 1684–1688.

Neogi, S., S. Dasgupta, and M. Fukuoka (1998), High P–T polymetamorphism, dehydration melting, and generation of migmatites and granites in the Higher Himalayan crystalline complex, Sikkim, India, *J. Petrol.*, *39*, 61–99.

Norlander, B. H., D. L. Whitney, C. Teyssier, and O. Vanderhaeghe (2002), Partial melting and decompression of the Thor-Odin dome, Shuswap metamorphic core complex, Canadian Cordillera, *Lithos*, *61*, 103–125.

Pan, G., J. Ding, D. Yao, and L. Wang (2004), Geological map of Qinghai-Xiang (Tibet) plateau and adjacent areas (1:1,500,000), Chengdu Institute of Geology and Mineral Resources, China Geological Survey, Chengdu Cartographic Publishing House, Chengdu, China.

Quigley, M.C., Y. Liangjun, C. Gregory, A. Corvino, M. Sandiford, C. J. L. Wilson, and L. Xiaohan (2008) U-Pb SHRIMP zircon geohchronology and T-t history of the Kampa Dome, southern Tibet, *Tectonophysics*, *446*, 97–113.

Ratschbacher, L., W. Frisch, and G. Lui (1994), Distributed deformation in southern and western Tibet during and after the India-Asia collision, *J. Geophys. Res.*, *99*, 19917–19945.

Ratschbacher, L., I. Krumrei, M. Blumenwitz, M. Staiger, R. Gloaguen, B. V. Miller, S.D. Samson, M.A. Edwards, and E. Appel (2011), Rifting and strike-slip shear in central Tibet and the geometry, age and kinematics of upper crustal extension in Tibet, *Spec. Publ. Geol. Soc. Lond.*, *353*, 127–163, doi:10.1144/SP353.8.

Reiners P. W., and M. T. Brandon (2006), Using thermochronology to understand orogenic erosion, *Annu. Rev. Earth Planet. Sci.*, *34*, 419–466.

Rolfo, F., R. Carosi, C. Montomoli, and D. Visonà (2008), Discovery of granulitized eclogite in North Sikkim expands the Eastern Himalaya high-pressure province, *Himalayan J. Sci.*, *5*, 126–127.

Rowley, D. B. (1996), Age of initiation of collision between India and Asia: A review of stratigraphic data, *Earth Planet. Sci. Lett.*, *145*, 1–13.

Rubatto, D., J. Hermann, A. Berger, and M. Engi (2009), Protracted fluid-induced melting during Barrovian metamorphism in the Central Alps, *Contrib. Mineral. Petrol.*, doi: 10.1007/s00410-009-0406-5.

Rubatto, D., S. Chakraborty, and S. Dasgupta (2012), Timescales of crustal melting in the Higher Himalayan Crystallines (Sikkim, Eastern Himalaya) inferred from trace element-constrained monazite and zircon chronology, *Contrib. Mineral. Petrol.*, doi:10.1007/s00419-012-0812-y.

Sakai, H., M. Sawada, Y. Takigami, Y. Orihashi, T. Danhara, H. Iwano, Y. Kuwahara, Q. Dong, H. Cai, and J. Li (2005), Geology of the summit limestone of Mount Qomolangma (Everest) and cooling history of the Yellow Band under the Qomolangma detachment, *Island Arc*, *14*, 297–310.

Schärer, U. (1984), The effect of initial ^{230}Th disequilibrium on young U/Pb ages: the Makalu case, Himalaya, *Earth Planet. Sci. Lett.*, *67*, 191–204.

Schelling, D. (1992), The tectonostratigraphy and structure of the eastern Nepal Himalaya, *Tectonics*, *11*, 925–943.

Searle, M., R. Simpson, R. Law, R. Parrish, and D. Waters (2003), The structural geometry, metamorphic and magmatic evolution of the Everest massif, High Himalaya of Nepal–South Tibet, *J. Geol. Soc. Lond.*, *160*, 345–366.

Simpson, R. L., R. R. Parrish, M. P. Searle, and D. J. Waters (2000), Two episodes of monazite crystallization during metamorphism and crustal melting in the Everest region of the Nepalese Himalaya, *Geology*, *28*, 403–406.

Spear, F. S. and J. M. Pyle (2002), Apatite, monazite, and xenotime in metamorphic rocks, *Rev. Mineral. Geochem.*, *48*, 293–335.

Stockli, D. F., K. A. Farley, and T. A. Dumitru (2000), Calibration of the apatite (U-Th)/He thermochronometer on an exhumed fault block, White Mountains, California, *Geology*, *28*, 983–986.

Streule, M. J., M. P. Searle, D. J. Waters, and M. S. A. Horstwood (2010), Metamorphism, melting, and channel flow in the Greater Himalayan Sequence and Makalu leucogranite: Constraints from thermobarometry, metamorphic modeling, and U-Pb geochronology, *Tectonics*, *29*, TC5011, doi:10.1029/2009TC002533.

Tailby, N.D., Walker, A.M., Berry, A.J., Hermann, J., Evans, K.A., Mavrogenes, J.A., H.St.C. O'Neill, I.S. Rodina, A.V. Soldatov, D. Rubatto, and S.R. Sutton (2011), Ti site occupancy in zircon, *Geochim. Cosmochim. Acta*, *75*, 905–921.

Teyssier, C. and D. L. Whitney (2002), Gneiss domes and orogeny, *Geology*, *30*, 1139–1142.

Vance, D., W. Müller, and I. M. Villa (2003), Geochronology: linking the isotopic record with petrology and textures—an introduction, *Spec. Publ. Geol. Soc. Lond.*, *220*, 1–24.

Vannay, J. C. and K. Hodges (1996), Tectonometamorphic evolution of the Himalayan metamorphic core between the Annapurna and Dhaulagiri, central Nepal, *J. Metamorph. Geol.*, *14*, 635–656.

Visoná, D., R. Carosi, C. Montomoli, M. Tiepolo, and L Peruzzo (2012), Miocene andalusite leucogranite in central-east Himalaya (Everest-Masang Kang area): Low-pressure melting during heating, *Lithos*, *144–145*, 194–208.

Wagner, T., J. Lee, B. R. Hacker, and G. Seward (2010), Kinematics and vorticity in Kangmar Dome, southern Tibet: Testing midcrustal channel flow models for the Himalaya, *Tectonics*, *29*, TC6011, doi:10.1029/2010TC002746.

Warren, C., C. Beaumont, and R. Jamieson (2008), Modelling tectonic styles and ultra-high pressure (UHP) rock exhumation during the transition from oceanic subduction to continental collision, *Earth Planet. Sci. Lett.*, *267*, 129–145.

Warren, C., D. Grujic, D. A. Kellett, J. Cottle, R. Jamieson, and K. Ghalley (2011a), Probing the depths of the India-Asia collision: U-Th-Pb monazite chronology of granulites from NW Bhutan, *Tectonics*, *30*, 1–24.

Warren, C.J., D. Grujic, J.M. Cottle, and N.W. Rogers (2011b), Constraining cooling histories: rutile and titanite chronology and diffusion modeling in NW Bhutan, *J. Metamorph. Geol.*, doi: 10.1111/j.1525-1314.2011.00958.

Watson, E. and T. Harrison (2005), Zircon thermometer reveals minimum melting conditions on earliest Earth, *Science*, *308*, 841–844.

Watson, E., D. Wark, and J. Thomas (2006), Crystallization thermometers for zircon and rutile, *Contrib. Mineral. Petrol.*, *151*, 413–433.

Webb, A.A.G., A. Yin, T.M. Harrison, J. Célérier, and W.P. Burgess (2007), The leading edge of the Greater Himalayan Crystalline complex revealed in the NW Indian Himalaya: Implications for the evolution of the Himalayan orogen, *Geology*, *35*, 955–958.

Webb, A.A.G., A.K. Schmitt, D. He, and E.L. Weigand (2011), Structural and geochronological evidence for the leading edge of the Greater Himalayan Crystalline complex in the central Nepal Himalaya, *Earth Planet. Sci. Lett.*, *304*, 483–495.

Whitney, D. L. and B. W. Evans (2010), Abbreviations for names of rock-forming minerals, *Am. Mineral.*, *95*, 185–187.

Whitney, D. L., C. Teyssier, and A. K. Fayon (2004), Isothermal decompression, partial melting and exhumation of deep continental crust, *Spec. Publ. Geol. Soc. Lond.*, *227*, 313–326.

Wolf, R. A., K. A. Farley, and D. M. Kass (1998), Modeling of the temperature sensitivity of the apatite (U-Th)/He thermochronometer, *Chem. Geol.*, *148*, 105–114.

Wu, C., K. Nelson, G. Wortman, S. D. Samson, Y. Yue, J. Li, W. Kidd, and M. Edwards (1998), Yadong cross structure and South Tibetan Detachment in the east central Himalaya (89°-90°), *Tectonics*, *17*, 28–45.

Zhang, J. and L. Guo (2007), Structure and geochronology of the southern Xainza-Dinggye rift and its relationship to the south Tibetan detachment system, *J. Asian Earth Sci.*, *29*, 722–736.